N84-25481

MRI REPORT

# CONTAINERLESS HIGH TEMPERATURE PROPERTY MEASUREMENTS BY ATOMIC FLUORESCENCE

FINAL TECHNICAL REPORT
May 1984

NASA Contract No. NAS8-34383
MRI Project No. RA-314-G

Prepared for

Materials Processing in Space Program
Contract Monitor: L. B. Gardner, JA64
NASA-George C. Marshall Space Flight Center
Marshall Space Flight Center, Alabama 35812

**MRI** WASHINGTON, D.C. 20006–Suite 250, 1750 K Street, N.W. • 202 293-3800

NASA SCIENTIFIC AND TECHNICAL INFORMATION FACILITY
Operated by PRC Data Services Company
POST OFFICE BOX 8757 BALT/WASH INTERNATIONAL AIRPORT, MARYLAND 21240 TELEPHONE (301) 796-5300

**COMMUNICATION/ROUTING TRANSCRIPT**

**ACTION CODES**

1-YOUR ACTION
2-YOUR APPROVAL
3-FILE
4-INFORMATION
5-INVESTIGATE & ADVISE
6-NOTE & FORWARD
7-NOTE & RETURN
8-PER REQUEST
9-RECOMMENDATION
10-YOUR SIGNATURE

| COST CENTER | NAME | LOCATION | ACTION CODE |
|---|---|---|---|
| | Thelma Tillery-Mosley | | 1 |
| | cc: J. Freeman | | |
| | M. Streeks | | |
| | | | |
| | | | |

Please make the following data changes:

N84-25342
title (utl)
change 4) to 40

N84-25481
abstract (abs)
change Ai203 to Al203

N84-24602
abstract (abs)
change is reviewed to are reviewed

N84-24806
title (utl)
change polytetrafluorethylene to polytetrafluoroethylene

N84-24543
abstract (abs)
change matri to matrix

**FROM**

| COST CTR: | NAME: | LOCATION: | DATE: |
|---|---|---|---|
| | | | |

FF489 JUN 80

# CONTAINERLESS HIGH TEMPERATURE PROPERTY MEASUREMENTS BY ATOMIC FLUORESCENCE

FINAL TECHNICAL REPORT
May 1984

NASA Contract No. NAS8-34383
MRI Project No. RA-314-G

Prepared for

Materials Processing in Space Program
Contract Monitor: L. B. Gardner, JA64
NASA-George C. Marshall Space Flight Center
Marshall Space Flight Center, Alabama 35812

**MIDWEST RESEARCH INSTITUTE** 425 VOLKER BOULEVARD, KANSAS CITY, MISSOURI 64110 ∘ 816 753-7600

## PREFACE

This is the final technical report for NASA Contract No. NAS8-34383 with Yale University. Since November 1, 1982, a portion of the work, including reporting requirements, has been subcontracted by Yale University to Midwest Research Institute, where the principal investigator, P. C. Nordine, is now employed. Dr. R. A. Schiffman and Prof. C. A. Walker of Yale University are co-principal investigators for the contract.

Dr. Nordine is the appropriate contact concerning technical and administrative questions about the work.

Approved for:

MIDWEST RESEARCH INSTITUTE

A. E. Vandegrift, Ph.D.
Acting Director
Center for Materials Science

May 1984

TABLE OF CONTENTS


| | | Page |
|---|---|---|
| I. | Introduction | 1 |
| | 1. $Al_2O_3$ (sapphire and alumina) Evaporation | 1 |
| | 2. Gas Density Thermometry | 1 |
| | 3. Properties of Levitation Jets | 2 |
| | 4. Molybdenum Evaporation | 2 |
| | 5. Tungsten Evaporation | 2 |
| | 6. Radiative Lifetimes and Collisional Energy Transfer Rates | 3 |
| | 7. $LaB_6$ Evaporation | 3 |
| II. | Experimental | 4 |
| III. | Results | 8 |
| | 1. Hg-Atom Fluorescence Study of the Aerodynamic Levitation Jet | 8 |
| | 2. Al-Atom Fluorescence: Sapphire and Alumina Evaporation | 15 |
| | 3. Hg-Atom Fluorescence Gas Thermometry | 23 |
| | 4. Molybdenum Evaporation | 26 |
| | 5. Tungsten Evaporation | 29 |
| | 6. Radiative Lifetimes and Collisional Energy Transfer Rates | 35 |
| | 7. $LaB_6$ Evaporation | 40 |
| IV. | Discussion | 47 |
| | 1. Temperature Measurement | 47 |
| | 2. Tungsten and Molybdenum Evaporation | 49 |
| | 3. $LaB_6$ Evaporation | 49 |
| | 4. Containerless Equilibrium Component Activity Measurements | 50 |
| V. | References | 52 |
| VI. | Publications and Presentations | 55 |
| VII. | Distribution | 56 |

## List of Figures


| Figure | Title | Page |
|---|---|---|
| 1a | Side View of the Experiment | 5 |
| 1b | Top View of the Apparatus | 5 |
| 2 | Hg-Atom Fluorescence Intensity Versus Detector Aperture Height for Two Laser Trigger to Signal Measurement Interval Delay Times | 9 |
| 3 | Hg-Atom Fluorescence Image Height Versus Signal Detection Delay Time | 10 |
| 4 | Radial Variation of Concentration in a Free Jet at Different Ambient Pressures | 11 |
| 5 | Density at Jet Center Versus Ambient Pressure | 12 |
| 6 | Axial Variation of Hg-Seed Atom Concentration in a Supersonic Free Jet of Argon Gas | 13 |
| 7 | Laser Induced Hg-Atom Fluorescence Photographs of Supersonic Free Jets of Mercury Seeded Argon Gas | 14 |
| 8 | Radial Variation of Free Jet Velocity | 16 |
| 9 | Al-Atom Fluorescence Intensity Versus Apparent Temperature for Laser Heated Sapphire Filament | 18 |
| 10 | Al-Atom Fluorescence Intensity Versus Apparent Temperature for Levitated Spheres | 19 |
| 11 | Al-Atom Fluorescence Intensity versus Apparent Temperature for Levitated 4 mm and 5 mm Sapphire Spheres | 20 |
| 12 | Al-Atom Fluorescence Intensity versus Apparent Temperature for Levitated 3.18 mm Polycrystalline Alumina (A,B) and Sapphire (C,D) Spheres | 22 |
| 13 | Al-Atom Fluorescence Intensity Versus Height Above a Levitated Sapphire Sphere | 24 |
| 14 | Test of Hg-Atom Fluorescence Thermometry | 25 |
| 15 | Temperature Dependence of Mo ($^7S_3$) Ground State Fluorescent Intensity over Electromagnetically Levitated, CW $CO_2$ Laser Heated Molybdenum Spheres, in Vacuum | 27 |
| 16 | Partial Energy Level Diagram for Atomic Tungsten | 30 |

TABLE OF CONTENTS (continued)


| Figure | Title | Page |
|---|---|---|
| 17 | Temperature Dependence of Fluorescence Intensity for W ($^5D_1$) Ground State Atoms in the Wake of an Electrically Heated Tungsten Filament | 31 |
| 18 | Temperature Dependence of Fluorescent Intensity for Five Electronic States of Atomic Tungsten in the Wake of Electrically Heated Tungsten Filaments | 32 |
| 19 | Measurement of the $^3P_0$:$^5D_0$ Fluorescence Intensity Ratio | 33 |
| 20 | Transitions of Tungsten $^7D_1^0$ and $^7F_2^0$ Atoms | 37 |
| 21 | LIF Intensity versus Delay Time for Emission by Tungsten $^7D_1^0$ and $^7F_2^0$ Atoms | 38 |
| 22 | Temperature Dependence of Boron and Lanthanum LIF Intensities over an Aerodynamically Levitated and CW $CO_2$ Laser Heated 0.28 cm Diameter $LaB_6$ Sphere | 41 |
| 23 | Axial Boron-Atom Concentration Gradient in the Wake of a Levitated $LaB_6$ Sphere | 43 |
| 24 | Radial Variation of Boron-Atom Concentration | 43 |


List of Tables


| Table | Title | Page |
|---|---|---|
| 1 | Atom Pressures and Specimen Temperatures | 6 |
| 2 | Species Detected by Laser Induced Fluorescence | 6 |
| 3 | Jet Momentum Flow Rate for the Experiments of Figure 4 | 16 |
| 4 | Tungsten Filament Evaporation Results | 34 |
| 5 | Measured and Literature Values for the Radiative Lifetimes of B, Mo, La, and W Atoms | 35 |
| 6 | Standard Enthalpy for the Reaction 1/7 $LaB_6(s)$ = 1/7 La(g) + 6/7 B(g) | 45 |
| 7 | Standard Enthalpy of Formation of $LaB_6$ | 46 |

# I. INTRODUCTION

This research is directed to the use of laser induced fluorescence (LIF) techniques for containerless study of high temperature processes and material properties. Gas jet and electromagnetic levitation and electromagnetic and laser heating techniques are used with LIF in earth-based containerless high temperature experiments. The work includes development of an apparatus and its use in studies of (a) chemical reactions on $Al_2O_3$, molybdenum, tungsten and $LaB_6$ specimens, (b) novel methods for noncontact specimen temperature measurement, (c) levitation jet properties and (d) radiative lifetimes and collisional energy transfer rates for electronically excited atoms. Brief summaries of these studies are given below. The apparatus is described in Section II and detailed results are presented in Section III.

Corrections to preliminary results reported in our two annual reports[1,2] are included in this final report. Recalibration of the optical pyrometers changes the molybdenum and tungsten intensity versus temperature data reported earlier. Better agreement is now obtained between measured and literature values for the evaporation enthalpies of these metals. The tungsten spectrum is sufficiently rich that it was necessary to recheck the identity of laser-induced tungsten atom and ion transitions. The data attributed to tungsten $^5D_0$ atoms (Figures 9, 10, and line 2 of Table 3, Ref. 2) were actually obtained on $^5D_1$ atoms by LIF at 384.62 nm rather than 384.75 nm. Also, the data in Ref. 2 attributed to tungsten ion LIF at 255.49 nm were actually obtained by exciting one of four tungsten atom $^5D_0$, $^5D_2$, and $^5D_3$ transitions that occur between 255.10 and 255.38 nm. No other errors occurred in the preliminary identification of species.

1. <u>$Al_2O_3$ (sapphire and alumina) evaporation</u>:[1,2] Al-atom evaporation from $Al_2O_3$ specimens was studied at temperatures up to 2327K, the melting point of $Al_2O_3$, using CW $CO_2$ laser heated sapphire and polycrystalline alumina specimens that were levitated in a gas jet and a self-supported sapphire filament specimen. The experiments yield accurate optical properties that are needed for temperature measurements. The emittance of alumina was found to increase with the ambient oxygen partial pressure. The effective emittance of nearly transparent sapphire is directly proportional to the specimen thickness. LIF sensitivity is sufficient that Al-atom concentrations as small as $2 \times 10^8$ $cm^{-3}$ can be measured with F-15 light collecting optics. A 100-fold increase in sensitivity would be possible if a small F-No lens were used to collect fluorescence.

2. <u>Gas density thermometry</u>:[1] A new method for noncontact temperature measurement on transparent specimens was demonstrated by adding mercury atoms to the Ar gas flow in which $Al_2O_3$ specimens were levitated and heated, and measuring Hg-atom concentrations near the specimen surfaces relative to the concentration under ambient conditions. The ambient temperature to high temperature Hg-atom concentration ratios (obtained by LIF) increase with specimen temperature and show a different dependence on apparent temperature for the two materials, due to their different emittances. When the optical properties of alumina and sapphire are taken into account, gas

density versus temperature functions are the same for both specimens. Thus, LIF measurements of gas density on a material of known emittance (and known temperature via optical pyrometry) yield a density versus temperature function that may subsequently be used to measure temperatures on materials whose optical properties are not known or change during a process.

The precision achieved in LIF gas density thermometry was about ±3%. The relation between ambient and high temperature Hg-atom concentration is influenced by the relative magnitudes of transport by convection and thermal diffusion. Reduced convection rates and smaller temperature gradients in space-based experiments would permit more precise and accurate use of this method than is possible on earth.

3. Properties of levitation jets: The most successful arrangement for high temperature gas jet levitation experiments employs a supersonic free jet to levitate the heated specimen.[3,4] The properties of such jets were studied by measuring LIF of Hg atoms added to the argon flow. Velocity measurements were achieved[1] by measuring the fluorescent image position versus delay time between laser excitation and fluorescence detection. The jet shock structure[2] was measured by laser induced fluorescence photography and by electronic measurement of the radial and axial variations of Hg-atom density in the jet. The results provide independent support for our earlier conclusions[3] about levitation jet behavior that were based on measurements of levitation height versus flow rate and pressure and on pitot tube measurements of jet properties. These results establish the sensitivity, precision, and spatial resolution with which velocities and nonuniform concentrations can be measured by these LIF techniques.

4. Molybdenum evaporation:[2] Molybdenum specimens were inductively levitated and laser heated in vacuum in the temperature range 2110 to 2790K. LIF intensity was measured versus temperature between 2260 and 2730K by exciting ground state $^7S_3$ Mo atoms to the $^3P_4^o$ level at $\lambda$ = 379.8 nm. The enthalpy of molybdenum evaporation to the atomic ground state, $\Delta H_T^o$ = 613 ± 15 kJ/g-mole, was derived from a plot of ln(IT) versus 1/T. This result is in good agreement with the value ($\Delta H_T^o$ = 631 ± 2 kJ/g-mole) derived from the accepted thermodynamic properties of molybdenum.[5] The intensity versus temperature data revealed that self-absorption of LIF occurs at the highest temperatures and a model of the self-absorption process was employed in the data reduction. Accurate self-absorption corrections are easily applied if this effect reduces LIF intensity by no more than a factor of two.

5. Tungsten evaporation:[1,2] Tungsten filament evaporation was studied in the temperature range 2700 to 3680K, the melting point of tungsten. The experiments were carried out in a flow of argon gas at p = 190 Pa. Ten different metastable electronic states of atomic W were detected and intensity versus temperature data obtained for six of these states. The average derived value for the enthalpy of solid tungsten evaporation to ground state atoms at T = 3070K was 831 ± 21 kJ/g-mole, in good agreement with the accepted value (825 ± 4 kJ/ g-mole) for this property.

The tungsten atom $^5D_0$:$^3P_0$ concentration ratios were obtained versus temperature by measuring fluorescence intensities when atoms in these states

were excited to the same upper level. The concentration ratios measured in this way are free from self-absorption and other effects that influence the relation between intensity and specimen vapor pressure. The correct $^5D_0$ - $^3P_0$ excitation energy was derived from the intensity ratio measurements. Such measurements provide a promising method by which the specimen temperature may be obtained if two lasers are used for simultaneous concentration measurements for two different atomic electronic states.

6. Radiative lifetimes and collisional energy transfer rates: Radiative lifetimes were measured for a variety of W-atom electronic states and for the B-, Mo-, and La-atom states from which LIF I(T) data were collected. The results for $^2S_{1/2}$ B-atoms and $^7P_4^0$ Mo-atoms agree well with literature values. No other lifetime data are available for comparison with our results

Laser trigger jitter interfered with accurate W-atom lifetime measurements. Thus, the results for short-lived states were upper limits of 10 or 20 ns. Lifetimes above ca. 100 ns were measured to about ±30%.

The energies of the W-atom $^7F_2^0$ and $^7D_1^0$ states differ by only 5 $cm^{-1}$ and their radiative lifetimes are sufficient that collisions with Ar atoms induce transitions between them. This energy transfer process was studied by observing the time-dependent emission from both states after laser excitation of either one. Limits on the radiative lifetimes and the rate constant for energy transfer were derived from the results.

7. $LaB_6$ evaporation:[22] Congruent evaporation of $LaB_6$ to atomic La and B was studied at temperatures up to 2530K, using CW $CO_2$ laser heated and aerodynamically levitated $LaB_6$ spheres. LIF intensities were measured versus temperature in the specimen wake. Axial and radial variations in the B-atom concentration were also measured in the specimen wake by spatially resolved LIF at constant specimen temperature. The B-atom concentration at temperatures above about 2300K was sufficient that self-absorption of LIF could be observed.

Absolute B-atom concentrations and third law enthalpies for the vaporization reaction were derived from the results. This was an iterative calculation in which the measured self-absorption effect depends on the thermodynamic properties used to extrapolate low temperature intensity data to the self-absorbing region. The derived standard enthalpy for the reaction:

$$1/7\ LaB_6(s) = 1/7\ La(g) + 6/7\ B(g)$$

was $\Delta H^o_{298}$ = 602.9 ± 5.9 kJ/mol. The error given for this result includes the experimental reproducibility (±2.0 kJ/mol), as well as contributions from uncertainty in temperature measurements, self-absorbing transition strength, the relation between boundary layer temperature and the measured boundary layer concentrations, the B:La diffusion coefficient ratio used to eliminate the La pressure in the thermodynamic analysis, and evaporation kinetic effects. $\Delta H^o_{v,298}$ (B) = 564.8 ± 7.2 kJ/mol is calculated from the present result, a calorimetric measurement of $\Delta H^o_{f,298}$ ($LaB_6$) and the standard enthalpy of La evaporation.

## II. EXPERIMENTAL

The apparatus used in this research is illustrated in Figures 1a and 1b, for which the components are identified in the figure captions. In the experiments reported, a pulsed dye laser was used to produce fluorescence from atomic mercury, aluminum, molybdenum, tungsten, lanthanum and boron. The Hg atoms were added to the argon flow. Al atoms were produced by evaporation from CW $CO_2$ laser heated and aerodynamically levitated sapphire and polycrystalline alumina spheres or self-supported sapphire filaments. Mo atoms were evaporated from solid spheres that were inductively levitated and laser heated in vacuum. W atoms were evaporated from electrically heated metal filaments. La and B atoms were evaporated from an aerodynamically levitated and laser heated $LaB_6$ sphere.

Electromagnetic induction levitation experiments with tungsten, molybdenum, and zirconium specimens were achieved. A 2.5 kW, 450 KHz power supply was used with levitation coil designs similar to those of Van Audenhove.[12] CW $CO_2$ laser heating of the levitated Mo and W specimens was also investigated. Levitated 2.5 mm diameter Mo spheres were just heated to the melting point at maximum laser power (ca. 300 W). Smaller Mo spheres were levitated at lower temperatures but became unstable and fell from the levitation coil as the temperature was increased. Stable levitation of tungsten could not be achieved at temperatures above about 3000K. Liquid Zr was levitated and electromagnetically heated to about 2400K, at which temperature the specimens fell from the levitation coil. Specimens larger than about 3 mm diameter were not investigated.

The apparatus includes a second harmonic generation cell (SHG cell) that doubles the dye laser output frequency for fluorescence studies at $\lambda$ = 220 - 360 nm. This cell is angle-tuned and efficiently doubles only the central component of the dye laser beam. Radiation diffracted from surfaces and apertures in the dye laser is not doubled by the SHG cell. The spatial mode of the frequency doubled beam is more perfect than that of the dye laser. The frequency doubled beam can thus be focused to a nearly diffraction limited spot, which is not possible with the direct dye laser beam, and superior spatial resolution in fluorescence intensity measurements was achieved only with the frequency doubled beam. A spatial filter could be used to obtain good focusing properties for the dye laser beam at all wavelengths.

Table 1 lists the atom vapor pressures and specimen temperatures under which LIF measurements were carried out. Even smaller vapor pressures (by about a factor of 100) could be measured with a smaller F-No light collecting lens. Electronic states of the detected species are given in Table 2, along with their electronic excitation energies and the laser wavelengths at which fluorescence was excited.

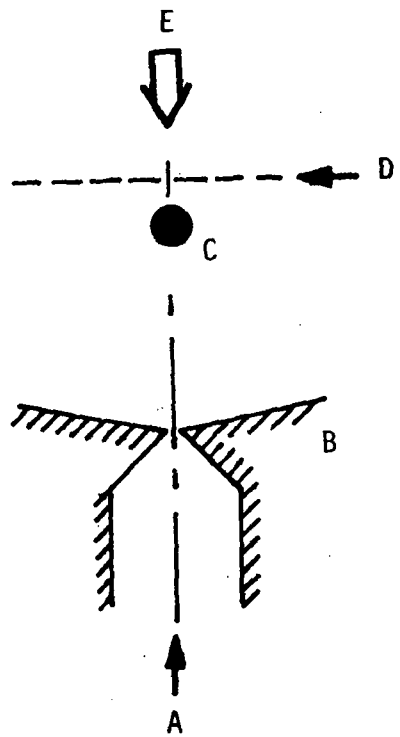


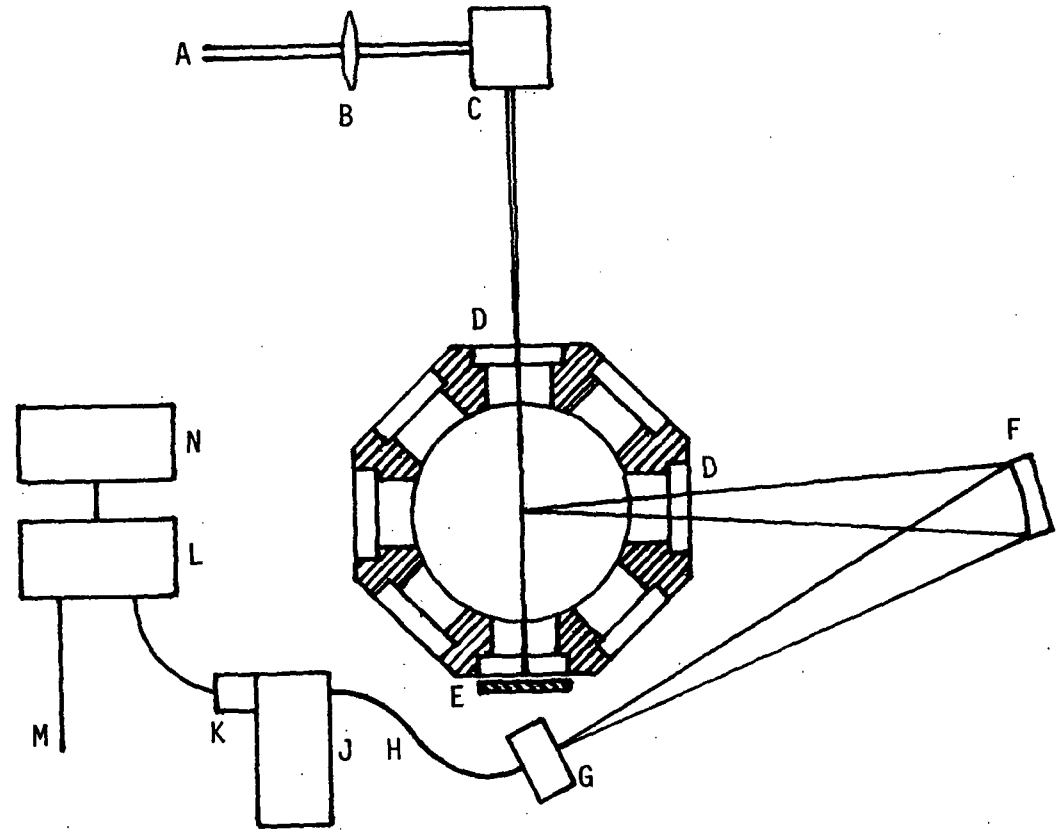


Figure 1a (left) - Side View of the Experiment. A - Ar flow, with added Hg, B - Nozzle with 0.082 cm diameter throat, C - Levitated specimen, D - Focused dye laser beam, E - CW $CO_2$ heating laser.

Figure 1b (right) - Top View of the Apparatus. A - Pulsed laser beam, B - Quartz lens, focal length = 50 cm, C - Beam steering device, D - Quartz windows, E - Laser beam stop, F - Front surface reflective lens, G - 0.40 mm aperture and positioning device, H - uv grade optical fiber, J - 1/4 m monochromator, K - Phototube, L - Boxcar averager, M - Trigger signal from laser, N - Chart recorder.

TABLE 1

ATOM PRESSURES[5] AND SPECIMEN TEMPERATURES

| Species | Pressure, atm. | Temperature (°K) |
|---|---|---|
| Al | 2.0E-10 to 1.0E-6 | 1830 - 2327 |
| Mo | 2.3E-9 to 1.6E-5 | 2110 - 2790 |
| W | 1.9E-9 to 5.0E-5 | 2700 - 3680 |
| Hg | < 4 E-7 | 298 - 2327 |
| B | 1.5E-8 to 2.5E-5 | 2000 - 2530 |
| La | 7.2E-9 to 1.2E-5 | 2000 - 2530 |

TABLE 2

SPECIES DETECTED BY LASER INDUCED FLUORESCENCE

| Species | Term[13] | Energy[13] (kJ/g-mole) | Laser Wavelengths[7] (nm) |
|---|---|---|---|
| Al | $^2P_{1/2}$ | 0 | 256.8, 265.2, 308.2, 394.4 |
| | $^2P_{3/2}$ | 1.3 | 257.5, 266.0, 309.3, 396.2 |
| Mo | $^7S_3$ | 0 | 379.8 |
| W | $^5D_0$ | 0 | 291.1, 384.7 |
| | $^5D_1$ | 20.0 | 384.6, 386.8, 400.5, 505.3, 505.4 |
| | $^7S_3$ | 35.3 | 381.7, 400.9, 404.6 |
| | $^5D_2$ | 39.8 | 255.1, 291.0, 383.5, 386.4, 484.4, 597.3 |
| | $^5D_3$ | 57.8 | 255.3, 255.4 |
| | $^5D_4$ | 74.4 | 396.5, 488.7, 500.6 |
| | $^3P_0$ | 114.0 | 402.9 |
| | $^3H_4$ | 145.5 | 397.5, 400.1 |
| | $^3G_3$ | 159.7 | 404.7, 405.5 |
| | $^3H_5$ | 180.3 | 407.3 |
| Hg | $^1S_0$ | 0 | 253.7 |
| B | $^2P_{1/2}$ | 0 | 249.7 |
| | $^2P_{3/2}$ | 0.19 | 249.8 |
| La | $^2D_{3/2}$ | 0 | 495.0, 497.8, 499.4, 515.9 |
| | $^2D_{5/2}$ | 12.6 | 272.6, 426.2, 428.0, 485.1, 490.1, 518.4 |
| | $^4F_{3/2}$ | 31.9 | 510.6 |
| | $^4F_{5/2}$ | 36.0 | 505.1 |
| | $^2D_{3/2}$ | 101.1 | 434.1 |

In a separate experiment, an F2.5 lens, 300 ± 100 nm interference filter (transmission > 50% at 253.7 nm) and a Polaroid camera (with Polaroid 084, ASA 3000 film) were used to obtain a photographic image of levitation jets by Hg-atom LIF. The laser beam was focused to a diameter ca. 0.025 cm at the center of the jet and swept up and down along the jet axis with the camera shutter open to expose the photograph.

## III. RESULTS

1. Hg-Atom fluorescence study of the aerodynamic levitation jet: The addition of atomic mercury to the argon stream allows the density and velocity of the levitation jet to be measured. Density is obtained, relative to the ambient density, from the ratio of the fluorescent intensity at the point of interest to that at a point outside the jet, under the known ambient conditions. Velocity can be determined[1] by measuring the location of the fluorescent image versus the delay time between a trigger signal from the laser and the interval sampled by the boxcar averager. Also, jet structure is observed by photographing the laser induced fluorescence obtained from axial scans of the laser beam along the jet axis.

Figure 2 presents the Hg fluorescence intensity versus height at the center of the jet for two different delay times, with the location of the focused dye laser beam fixed. It can be seen that the center of the fluorescent image moves about 0.1 mm when the delay time is increased 175 ns. The radiative lifetime of atomic Hg is 120 ns,[6] and the fluorescence intensity becomes too small for accurate measurement of the image profile at much longer delay times. Figure 3 plots several measurements of the location of the center of the fluorescent image versus delay time. A least-squares analysis gives the velocity, $u = 394 \pm 24$ m/s. Fewer height versus delay time data were obtained for most of the velocities reported below, and these velocity measurements are not as precise as that given in this example.

Figure 4 plots several measurements of the radial concentration variation in the jet, at fixed stagnation conditions but different ambient pressures. The density at the jet center was measured relative to the ambient density versus pressure to give the results in the bottom panel of Figure 5. The top panel of Figure 5 presents jet densities under nearly identical conditions that have been calculated from pitot tube measurements of the jet stagnation pressure (Ref. 3, Figure 7, curve No. 4). Fluorescence measurements under other conditions also give results that agree well with the pitot tube pressure measurements of Ref. 3.

Figure 5 reveals oscillations in the jet density with the ambient pressure that were not detected by the pitot tube measurements.[3] These variations of density with pressure are related to changes in the free jet shock structure that occur as the nozzle expansion ratio is changed.

Figure 6 presents the variation of density in the jet (relative to the ambient density) versus height, Z, above the nozzle. The free jet expansion process produces a strong shock at $Z \cong 3$ mm from the nozzle and a series of weaker shocks further downstream. Fluorescence photographs of the jet are presented in Figure 7, for nozzle stagnation pressures and pressure ratios stated in the figure caption. The argon flow rates (in g/sec) for these experiments equal $8.98 \times 10^{-7}$ times the nozzle stagnation pressures (in Pa). Figures 7a-c show the shock spacing, $\Delta Z$, increases as the nozzle pressure ratio ($p_0/p$) increases, in good agreement with the expected[8] result:

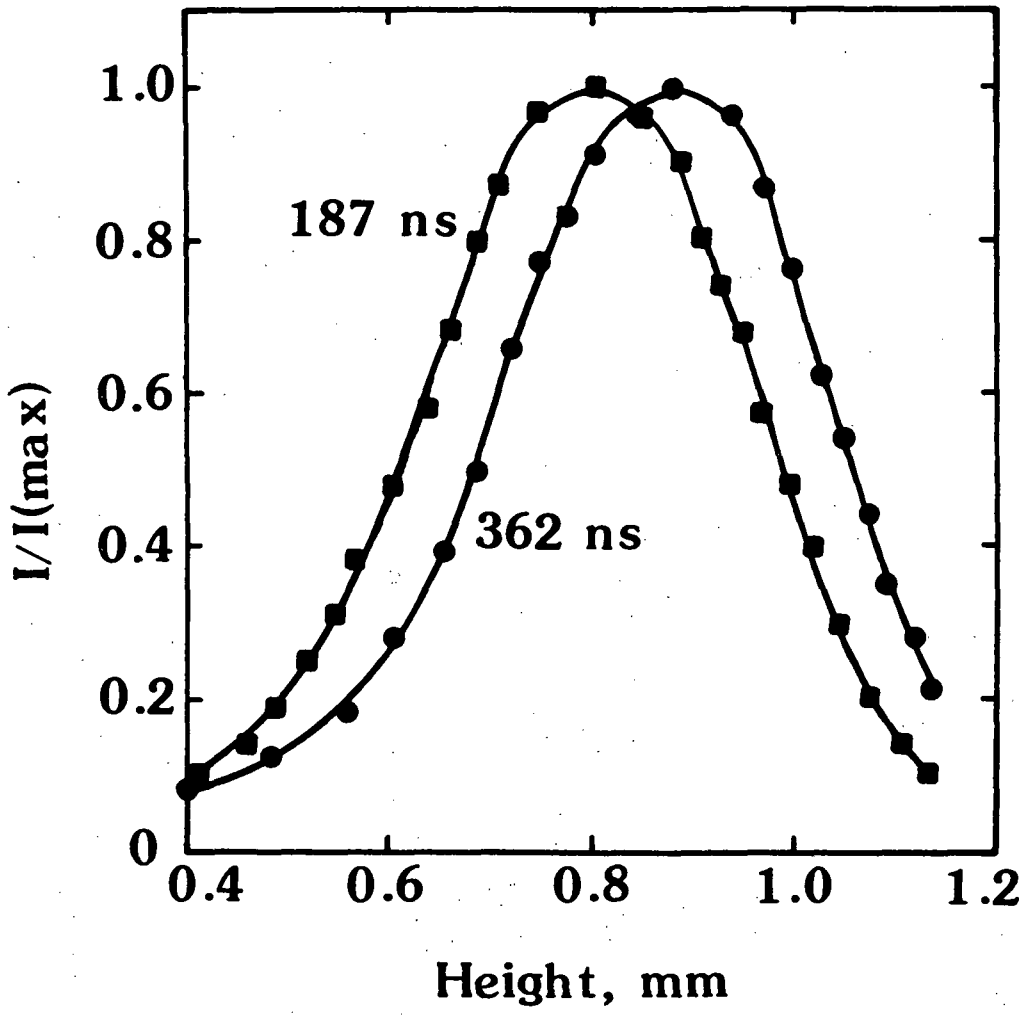


Figure 2 - Hg-Atom Fluorescence Intensity versus Detector Aperture Height for Two Delay Times Between Laser Trigger and Fluorescence Measurement. Conditions were: height above nozzle = 2.25 cm, Ar flow rate = 410 cc(STP)/min, p = 3.1 torr, nozzle stagnation pressure, $p_0$ = 77 torr.

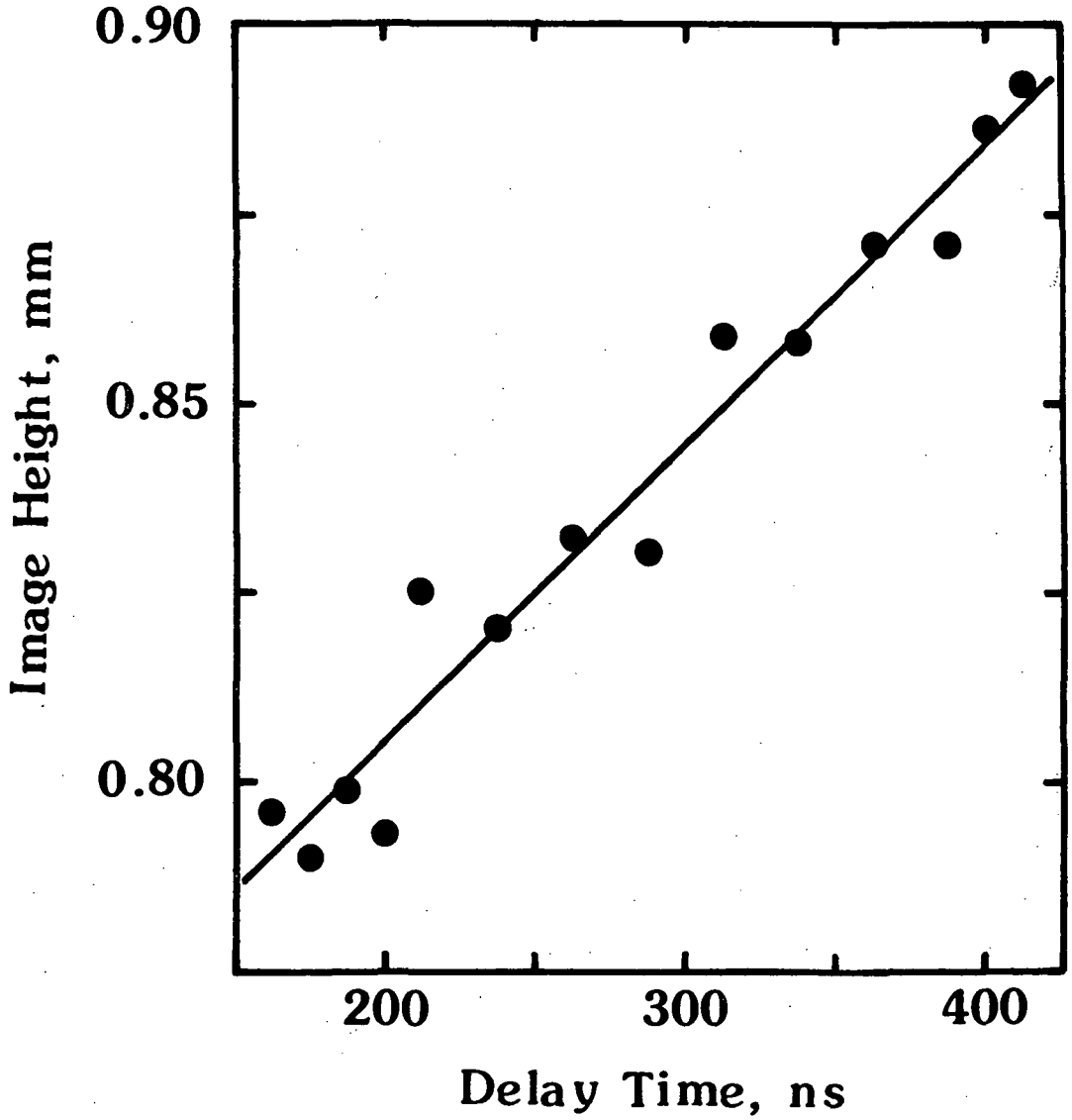


Figure 3 - Hg-Atom Image Height versus Signal Detection Delay Time. Slope = 394 ± 24 m/s. Conditions as in Figure 2.

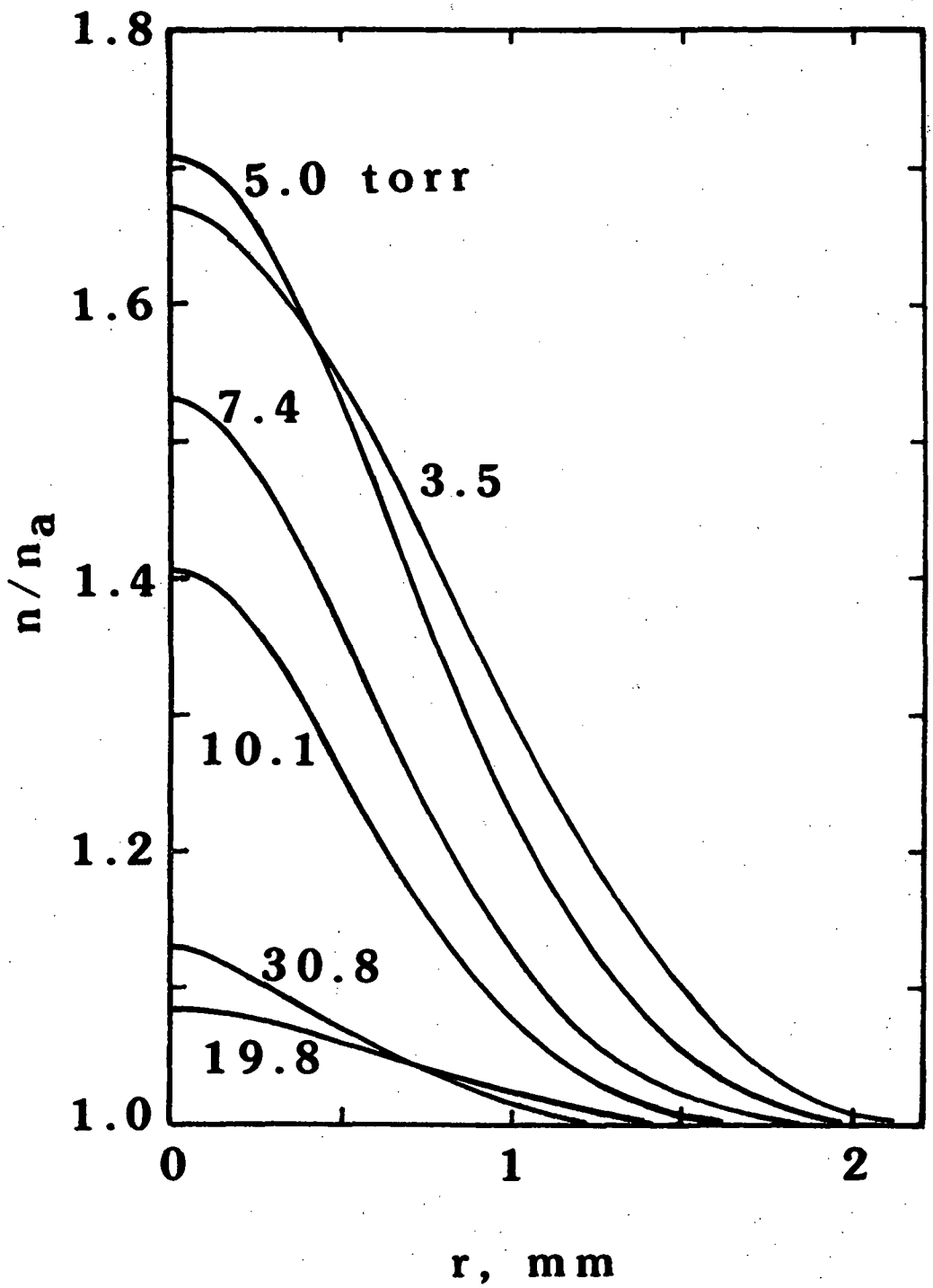


Figure 4 - Radial Variation of Concentration in a Free Jet at Different Ambient Pressures. Conditions are: height above nozzle = 2.00 cm, Ar flow rate = 455 cc (STP)/min, $p_0$ = 85 torr.

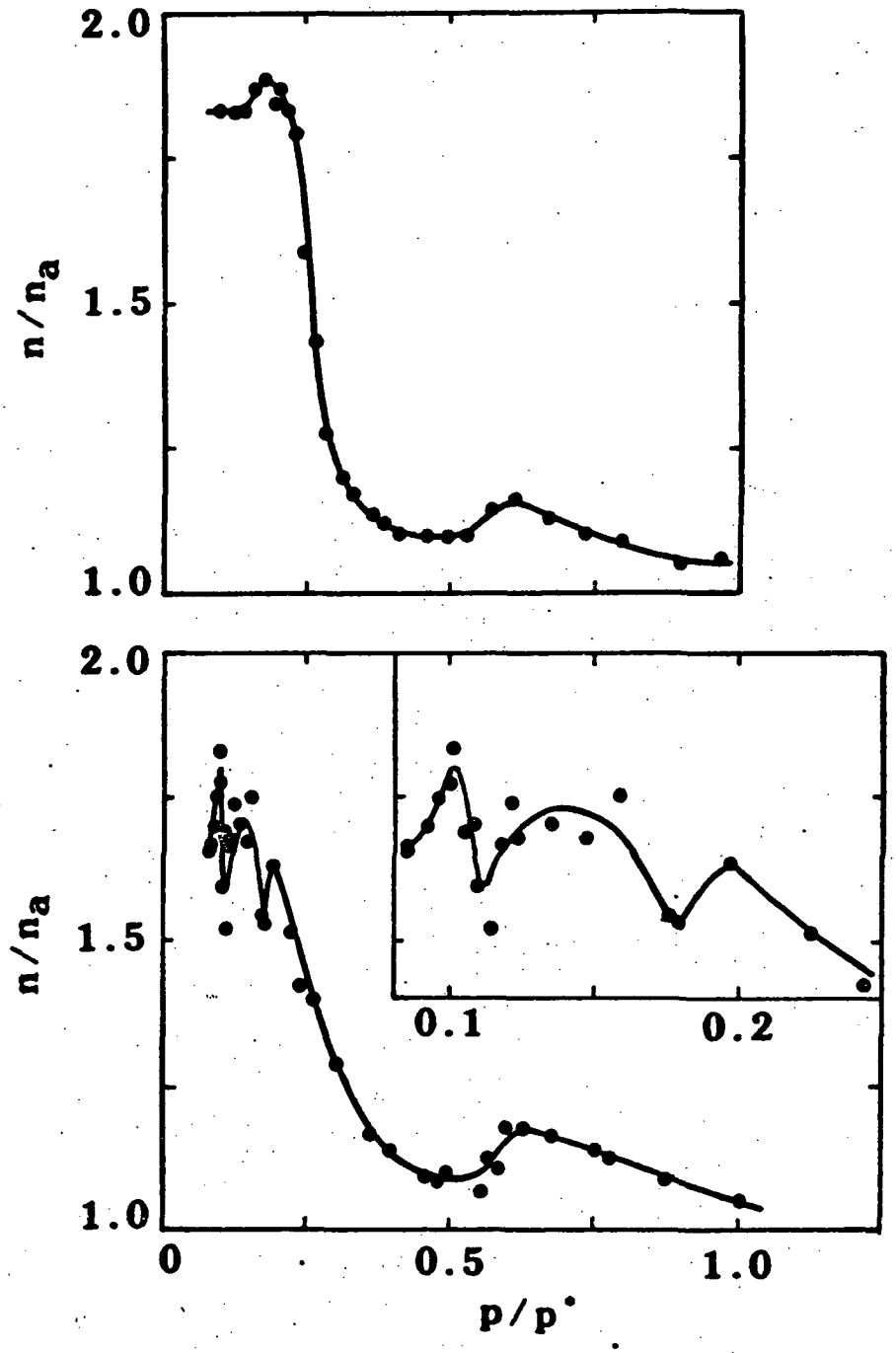


Figure 5 - Density at Jet Center versus Ambient Pressure. p* = pressure at (choked) nozzle. The upper panel gives data calculated from pitot tube measurements.[3] The lower panel and insert give measurements by the Hg-atom fluorescence technique.

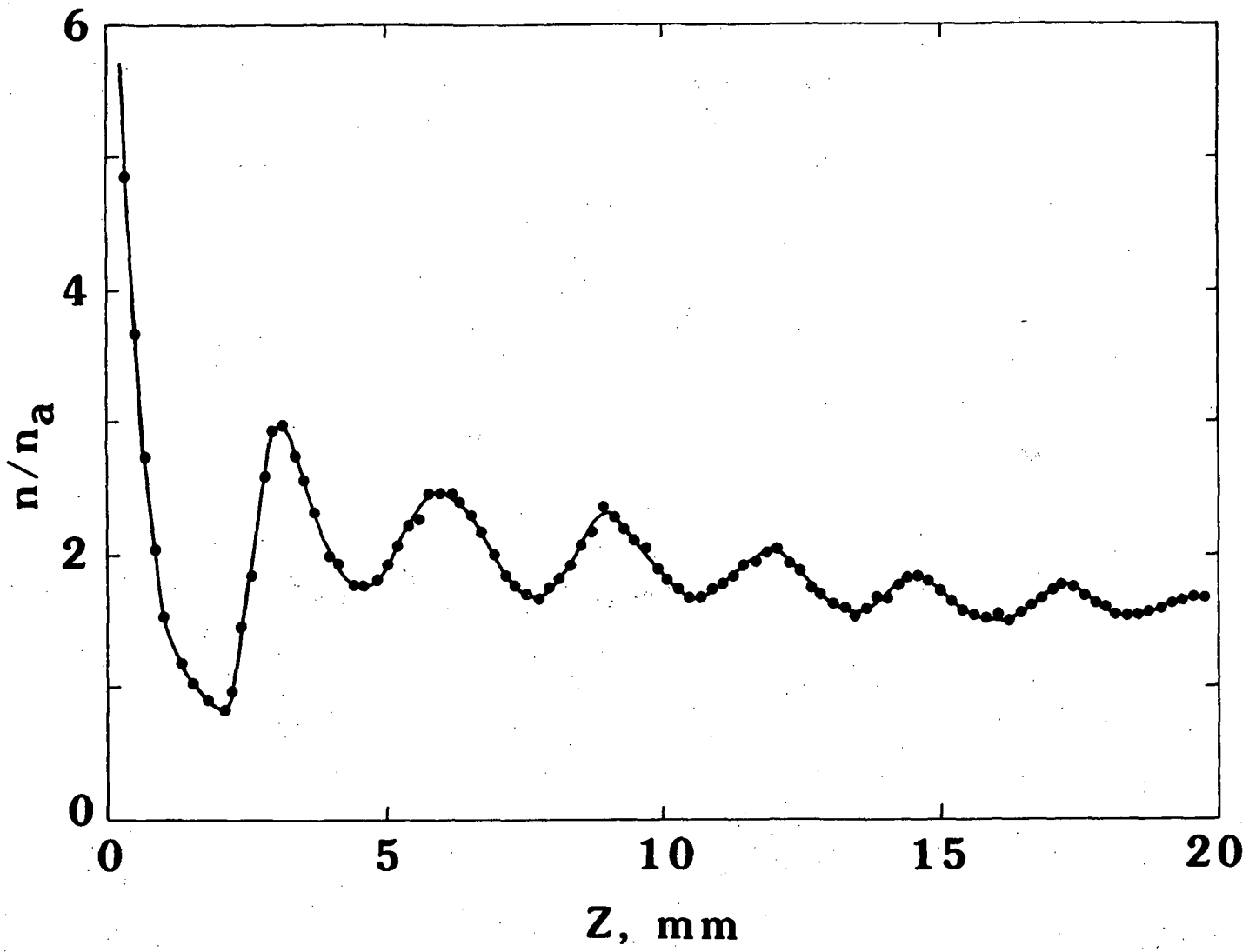


Figure 6 - Axial Variation of Hg-Seed Atom Concentration in a Supersonic Free Jet of Argon Gas. Conditions are: Ar flow rate = 13.6 mg/s, $P_o$ = 15,100 Pa, P = 460 Pa. The nozzle, whose effective diameter is 0.062 cm is located at z = 0.

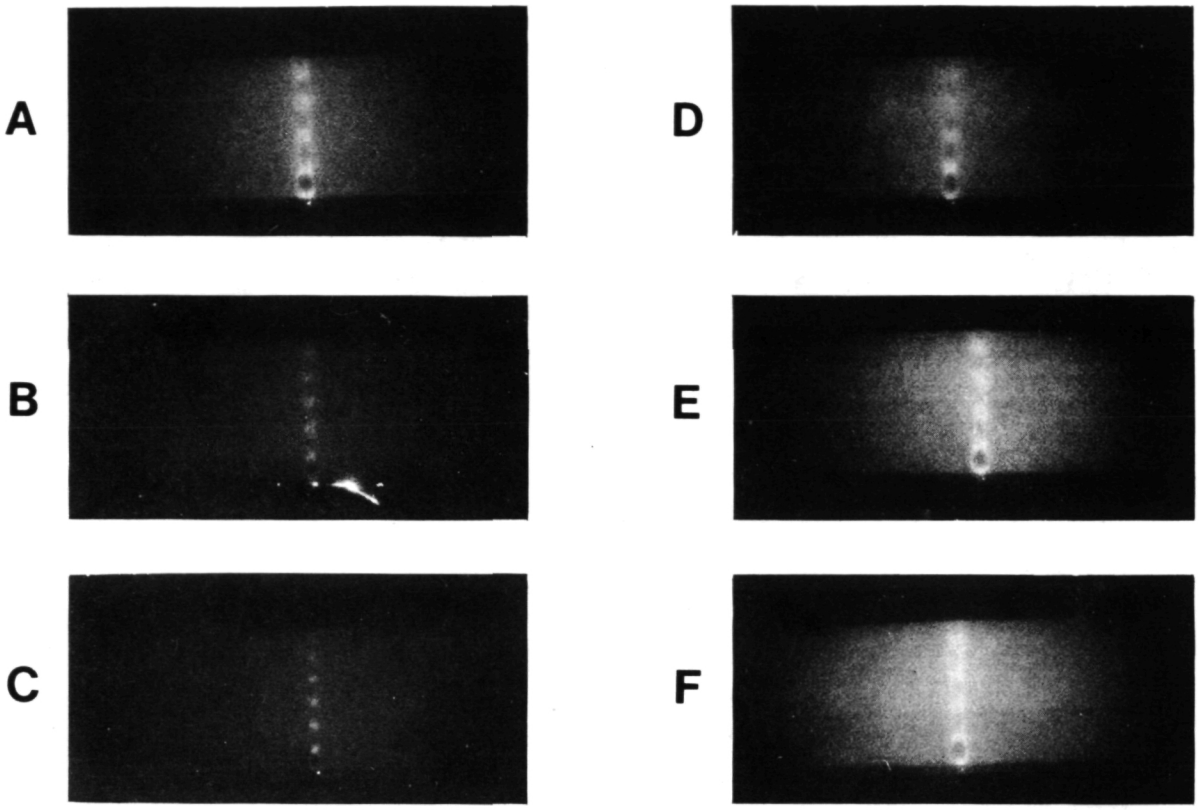


Figure 7 - Laser Induced Hg-Atom Fluorescence Photographs of Supersonic Free Jets of Mercury Seeded Argon Gas. Actual height of the imaged region was 1.34 cm. Reflection from the nozzle is apparent at the bottom of panel B. The effective nozzle throat diameter was 0.062 cm. Nozzle stagnation pressures (Pa): A,B,C,E - 15,000; D-7,400; F-27,500. Nozzle pressure ratios: A,D,E,F-33; B-21; C-15.

$$\Delta Z/d \cong 0.67\ (p_0/p)^{\frac{1}{2}} \qquad (1)$$

where d is the nozzle diameter (0.062 cm). The images in Figures 7A-C were obtained with a slightly larger flow rate than that required to levitate alumina spheres. Figures 7d-f illustrate the effects of flow rate on the jet structure at a constant nozzle pressure ratio. Although the shock spacing remains constant, the greater effects of viscosity at smaller flow rates are evident in the far field of the jets.

Figure 8 plots the radial variation in jet velocity that was obtained in two ways. The squares present direct measurements by the delayed fluorescence technique. The circles are calculated from density measurements and the assumptions that (a) the jet is adiabatic, (b) the pressure is uniform, and (c) the Hg-atom concentration is proportional to argon density, i.e., no heavy atom inertial separation effects occur in the free-jet expansion process, so that the Hg-atom mole fraction is uniform. The density-temperature product is then constant so the density measurements give local temperatures from the known ambient temperature. The velocity is then obtained from the gas kinetic energy, equal to $C_p(T_0 - T)$, where $T_0$ and T are the stagnation and jet temperatures, respectively. It can be seen that the jet velocity profile calculated under the above assumptions agrees well with that measured by the delayed fluorescence technique.

A further check can be made on the above analysis. If the pressure is uniform and equals the ambient pressure, the jet momentum flow rate is:

$$mu = m^*u^* + A^*(p^* - p) \qquad (2)$$

where * refers to choked conditions. The value of mu can also be calculated from:

$$mu = 2\pi \int_0^\infty \rho u^2 r dr \qquad (3)$$

where ρ is gas density. For this experiment, Eq. (2) gives mu = 791 g cm/sec$^2$ and Eq. (3) gives mu = 843 g cm/sec$^2$. When the same check is applied to the data of Figure 4, the results presented in Table 3 are obtained.

2. Al-Atom fluorescence: sapphire and alumina evaporation

a. Sapphire filament: Aerodyamically levitated spheres become unstable when they begin to melt. However, a self-supported sapphire filament can be partially melted. The effective total emittance of liquid $Al_2O_3$ is greater than that of the solid and laser power necessary to melt through a sapphire filament is about six times that required to bring the solid to the melting temperature. The effective spectral emittance of the liquid is also greater than that of the solid and the apparent temperature of a partially molten sapphire filament increases as the fraction of liquid material increases, at constant true temperature. These effects were studied by measuring the Al-atom florescence intensity in the wake of a laser

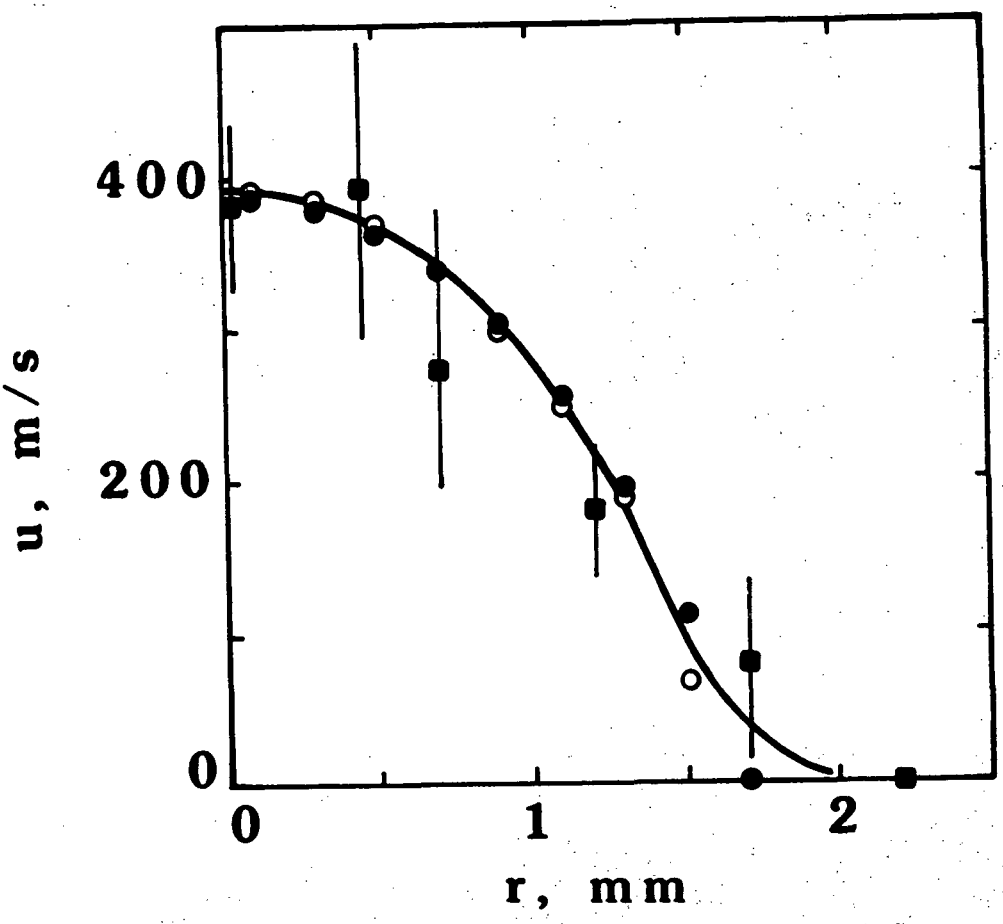


Figure 8 - Radial Variation of Free Jet Velocity. Squares give direct measurements by the delayed fluorescence technique. Circles are calculated from density measurements and assumptions that the flow is adiabatic, the pressure is uniform, and that no heavy atom (Hg)/light atom (Ar) separation effects occur. Conditions are: height above nozzle = 1.65 cm, Ar flow rate = 624 cc(STP)/min, $p_0$ = 115 torr, and p = 5.1 torr.

TABLE 3

JET MOMENTUM FLOW RATE FOR THE EXPERIMENTS OF FIGURE 4

| Pressure (torr) | Jet Momentum, g cm/sec$^2$ Eq. (2) | Eq. (3) | Value Ratio Eq. (2)/Eq. (3) |
|---|---|---|---|
| 3.4 | 584 | 553 | 1.06 |
| 5.0 | 576 | 641 | 0.90 |
| 7.4 | 563 | 579 | 0.97 |
| 10.1 | 548 | 499 | 0.95 |
| 19.8 | 495 | 273 | 1.81 |
| 30.8 | 435 | 365 | 1.19 |

heated sapphire filament versus apparent specimen temperature. The results are illustrated in Figure 9, which shows a nearly constant intensity at $T_a > 1480K$, where the specimen begins to melt. The small increase of intensity with apparent temperature above 1480K is mainly due to a larger evaporation coefficient for the liquid than for the solid and an increase in the evaporating area with the fraction of the specimen that is liquid, due to a volume difference between solid and liquid $Al_2O_3$.

b. Levitated sapphire and alumina spheres: The total emmittance of polycrystalline alumina is greater than that of sapphire. Thus, a greater heating laser power is necessary to bring an alumina sphere to a given temperature than is required for a sapphire sphere at the same temperature. At equal temperatures, the alumina sphere also has a greater spectral emittance and apparent temperature. But the vapor pressure at equal temperatures is the same for alumina and sapphire. The Al-atom fluorescent intensity in the wake of levitated 0.318 cm alumina and sapphire spheres is illustrated in Figure 10 as a function of apparent specimen temperature. For each specimen, a constant intensity is approached at the highest temperatures, when the specimen begins to melt. That is, the maximum intensities are achieved at the same true temperatures. The apparent temperature differences at equal true temperatures can thus be read from the Figure, at points where each specimen gave equal fractions of the maximum intensity.

The relation between specimen emittance, $\varepsilon$ true temperature, T, and apparent temperature, $T_a$ is:

$$1/T - 1/T_a = \lambda/C_2 \ln(\varepsilon) \qquad (4)$$

where $\lambda = 0.66$ micrometer is the effective pyrometer wavelength and $C_2 = 14388$ micrometer (degree K). The results of Figure 10 yield an effective alumina:sapphire emittance ratio equal to 16 for spheres of 0.318 cm diameter. Extrapolation of the linear lower temperature data on sapphire to the melting point gives an apparent melting temperature equal to 1460K, where the true temperature is 2327K.[9] The effective emittance of the sapphire sphere is thus about 0.0038, at temperatures above about 1800K. This value is less than would be calculated from the apparent melting temperature of the sapphire filament, probably because the sapphire filament contained internal voids that scatter light and produce a larger emittance than would be observed for a more perfect crystal.

Figure 11 presents intensity versus temperature data obtained with 4- and 5-mm sapphire specimens. The intensities have been adjusted so that the maximum intensity for the 4-mm specimen is twice that for the 5-mm specimen. The two curves are parallel and the reciprocal temperature difference at equal fractions of the maximum intensity is:

$$\Delta(1/T) = (1.1 + 0.1) \times 10^{-5} K^{-1} \qquad (5)$$

This result indicates that the emittance of sapphire is proportional to specimen thickness. Then the reciprocal temperature difference would be:

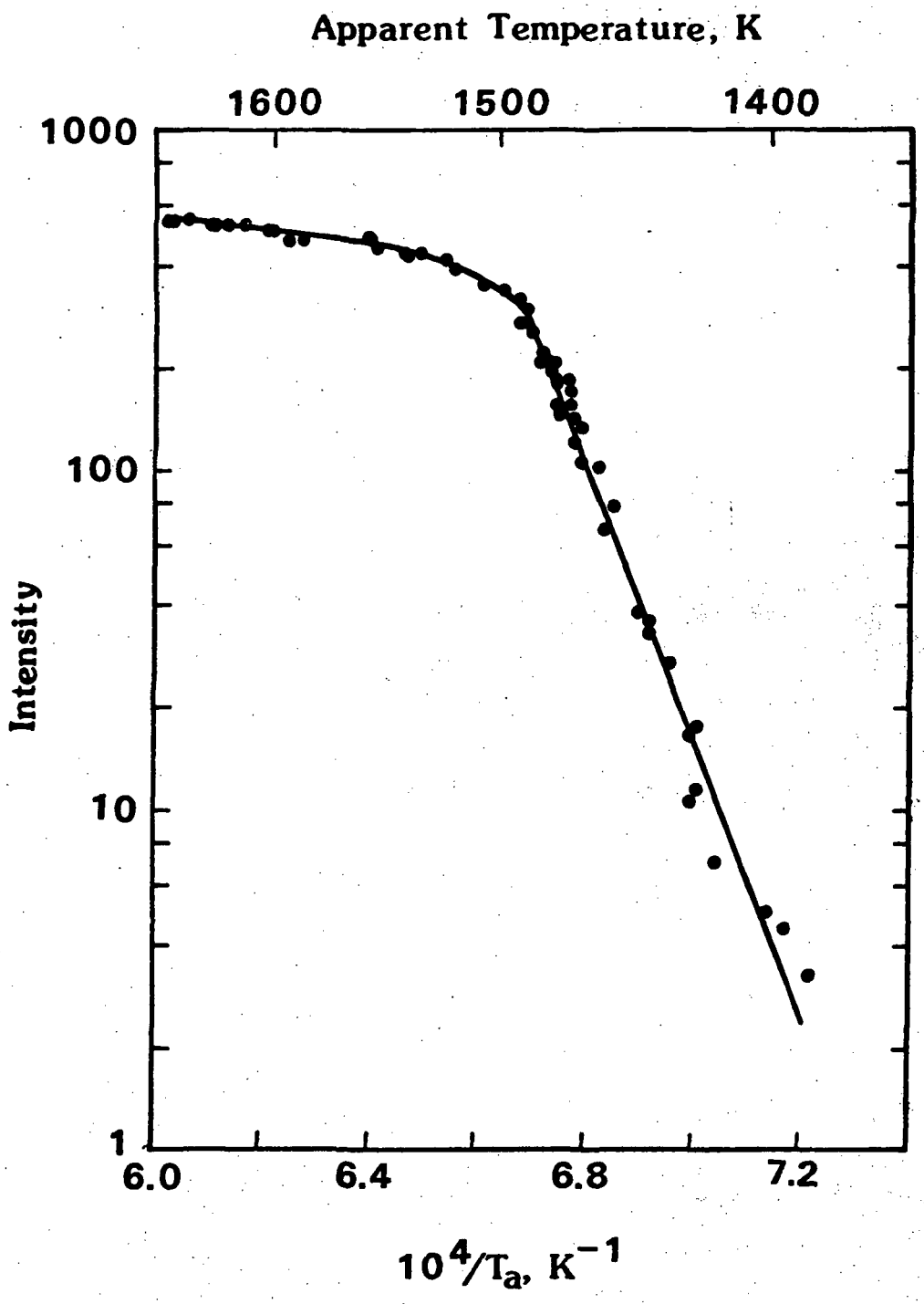


Figure 9 - Al-Atom Fluorescence Intensity versus Apparent Temperature for Laser Heated Sapphire Filament.

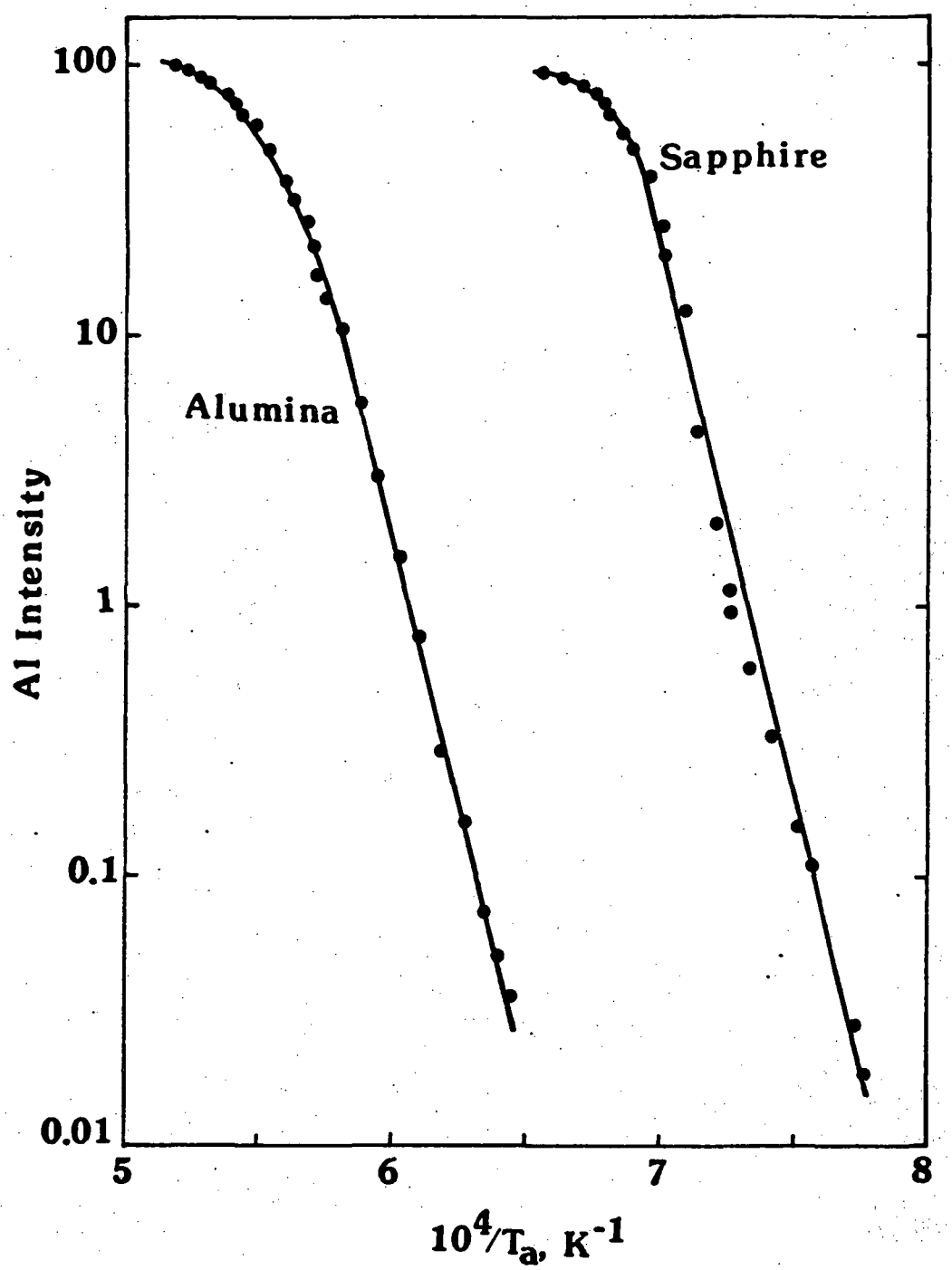


Figure 10 - Al-Atom Fluorescence Intensity versus Apparent Temperature for Levitated Spheres.

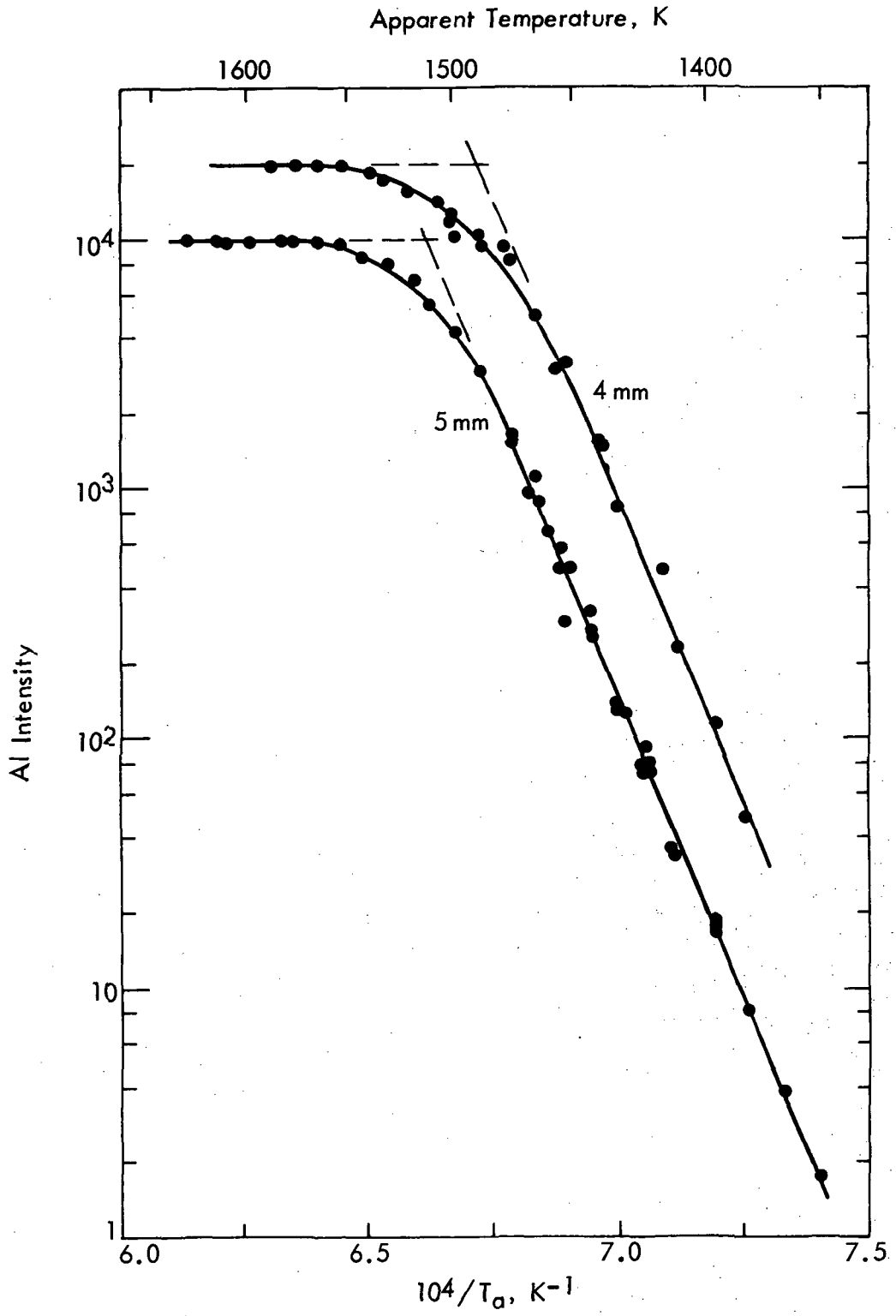


Figure 11 - Al-Atom Fluorescence Intensity versus Apparent Temperature for Levitated 4 mm and 5 mm Sapphire Spheres

$$\Delta(1/T) = (\lambda/C_2)\ \ln(d_2/d_1) \qquad (6)$$

With $\lambda = 0.66\ \mu$, $C_2 = 14{,}388\ \mu K$, $d_2 = 5$ mm, and $d_1 = 4$ mm, Eq. (6) gives $\Delta(1/T) = 1.02 \times 10^{-5}\ K^{-1}$, in agreement with the experimental result.

The slope of the ln(I) versus $1/T_a$ curves in Figure 11 is:

$$d\ \ln(I)/d(1/T_a) = -112{,}000\ K \qquad (7)$$

An approximate calculation which assumes that the major species (Al and O) are the only gaseous species over $Al_2O_3$* gives, from known thermodynamic properties:[9]

$$d\ \ln(I)/d(1/T) = -70{,}889\ K \qquad (8)$$

where intensity, I, is proportional to the equilibrium Al-atom concentration over $Al_2O_3$. The normal spectral emittance, $\varepsilon_\lambda$, of 5-mm sapphire is obtained from its apparent melting temperature, $T_a = 1511K$, the true melting temperature, $T = 2327K$,[9] and Eq. (4), which gives $\varepsilon_\lambda = 6.4 \times 10^{-3}$ at the melting point of the 5-mm sapphire sphere. From these results, we obtain:

$$1/T_a = 0.633/T + 3.90 \times 10^{-4}\ K^{-1} \qquad (9)$$

for the 5-mm specimen in the temperature range 1800 to 2327K. The emittance of sapphire spheres is then given by:

$$\varepsilon(\lambda = 0.66\ \mu)/d(cm) = 4.08 \times 10^{-4}\ \exp(8002/T). \qquad (10)$$

This result indicates that the spectral emittance of sapphire decreases with temperature above 1800K, in agreement with the spectral absorption coefficient measurements of Grvnak and Burch.[10] They found $K_\lambda = 0.036$/cm at 1973K and $K_\lambda = 0.028$/cm at 2273K (and $\lambda = 0.66\ \mu$). These values are in good agreement with absorption coefficients calculated from Eq. (10), with $\varepsilon/d \cong K_\lambda$.

Figure 12 presents intensity versus apparent temperature data for sapphire and alumina, measured in argon and in oxygen-seeded argon on the same specimens. The lower intensities observed in oxygen-seeded argon result from the reaction of evaporating Al atoms with gaseous $O_2$ in the region between the specimen surface and the point at which laser induced fluorescence is observed. The fractional intensity decrease should increase with the rate constant for $Al/O_2$ reaction. Since this decrease is constant for the sapphire experiment, it is clear that the $Al/O_2$ rate constant is nearly independent of temperature.

The apparent melting point derived for the oxygen-seeded sapphire experiment agrees with that in argon, but the apparent melting point of polycrystalline alumina increases from 1800 ± 20K in argon to 1890 ± 20K

---

* $AlO_2$, AlO, $Al_2O$, $Al_2O_2$, and $O_2$ are minor species[9] in the vapor over $Al_2O_3$.

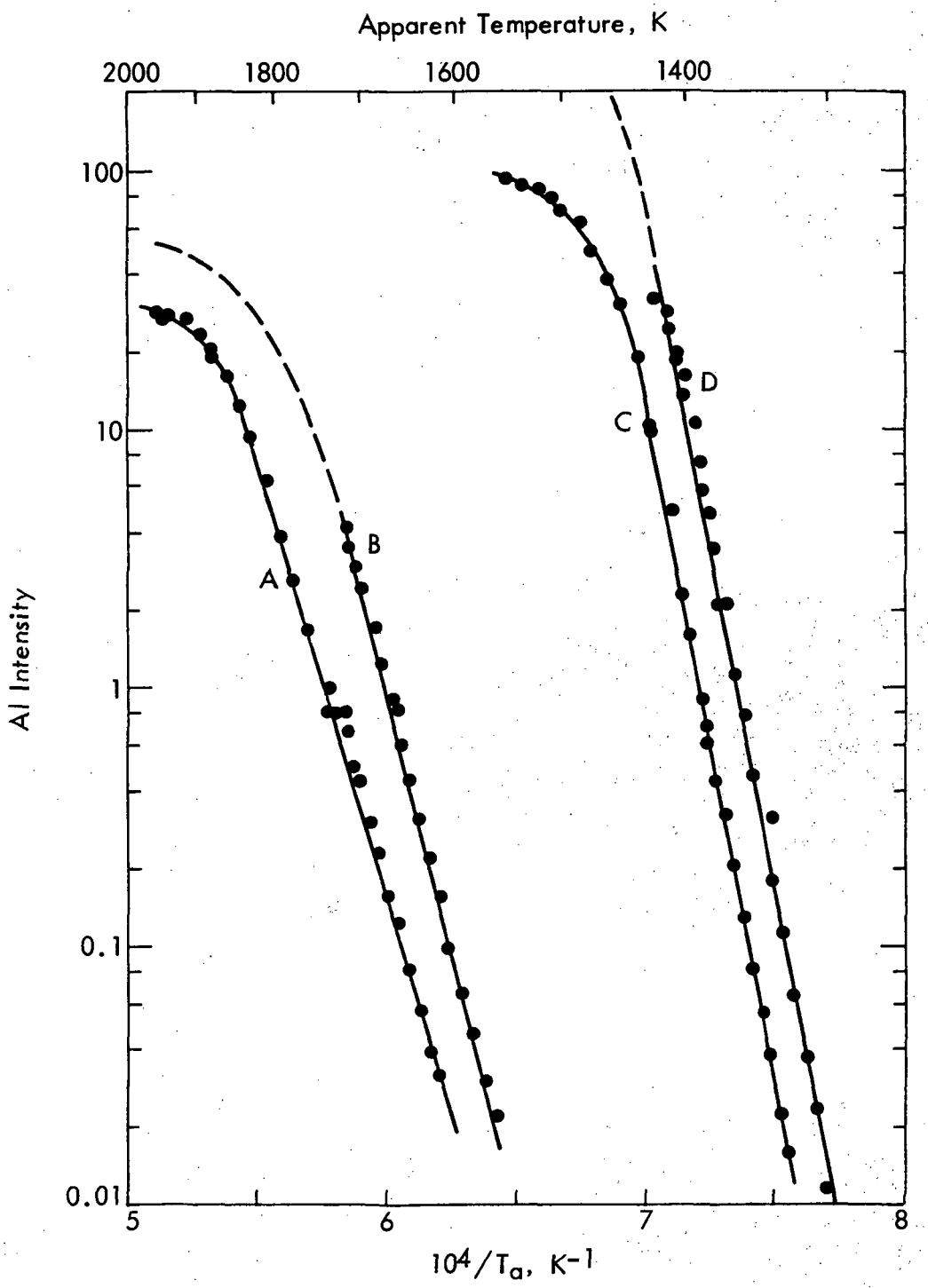


Figure 12 - Al-Atom Fluorescence Intensity versus Apparent Temperature for Levitated 3.18 mm Polycrystalline Alumina (A,B) and Sapphire (C,D) Spheres. A,C - $p(O_2) \cong 1Pa$. B,D - $p(O_2) = 0$.

in oxygen-seeded argon. Thus, it appears that the emittance of polycrystalline alumina depends on the ambient oxygen concentration. This result provides an explanation for the relatively low apparent melting temperatures for alumina in the present experiments, compared with the much higher value (2270 ± 20K) measured on laser heated alumina rods in air.[11]

c. Al atom reaction with ambient oxygen or water: It can be seen in Figure 12 that the Al atom fluorescence intensity is greater in pure argon than in oxygen seeded argon. In fact, the oxygen or water that outgasses from the surface of the apparatus is sufficient to produce a substantial decrease in Al-atom fluorescence intensity. For example, when a new alumina or sapphire specimen is first placed in the apparatus, the Al-atom intensities measured a few mm from the specimen surface in the wake of the heated specimen are 10 to 100 times less than would be expected. After overnight pumping on the apparatus, reproducable higher fluorescence intensities were obtained. However, if the Al-atom fluorescence intensity was measured versus height above the levitated specimen and extrapolated to the specimen surface, reproducible measurements were obtained. Thus, the decrease in Al-atom fluorescence intensity results from homogeneous reaction of oxygen or water with gaseous Al rather than a heterogeneous reaction of the specimen.

Figure 13 plots the variation of intensity with height above the specimen for different values of the ambient oxygen partial pressure that were set by adding oxygen to the levitating argon gas. The expected increase in the rate of Al consumption with the ambient oxygen concentration is observed. Unequal intensities at zero height do not occur after correction for small sensitivity differences between the experiments.

3. Hg-Atom fluorescence gas thermometry: In ideal gas thermometry, the gas densities at two points in an apparatus are measured under static conditions. With uniform pressure and a known value for one of the temperatures, the other temperature can be calculated because the product of density and temperature is constant for an ideal gas. The same principle can be used to measure very high temperatures that are not amenable to conventional ideal gas thermometry, using laser induced fluorescence to obtain the gas density ratio. In the experiments we have carried out, Hg-atom density ratios were measured, with Hg as the fluorescing seed gas in argon. Here, the product of Hg concentration and temperature cannot be assumed constant because thermal diffusion effects and inertial separation of heavy and light gases may occur.

The ambient Hg-atom fluorescence intensity was first measured under the flow conditions that occur in levitation experiments. Then sapphire and alumina spheres were levitated and heated, and the Hg-atom fluorescence intensity measured at a point 0.9 mm above the specimen in the specimen wake. The ambient to high temperature Hg-atom concentration ratios are plotted versus the apparent specimen temperature to ambient temperature ratios in Figure 14. The left panel gives the sapphire and alumina data at the apparent temperatures that were actually measured for these specimens. In the right hand panel of the figure, the sapphire data have been adjusted to

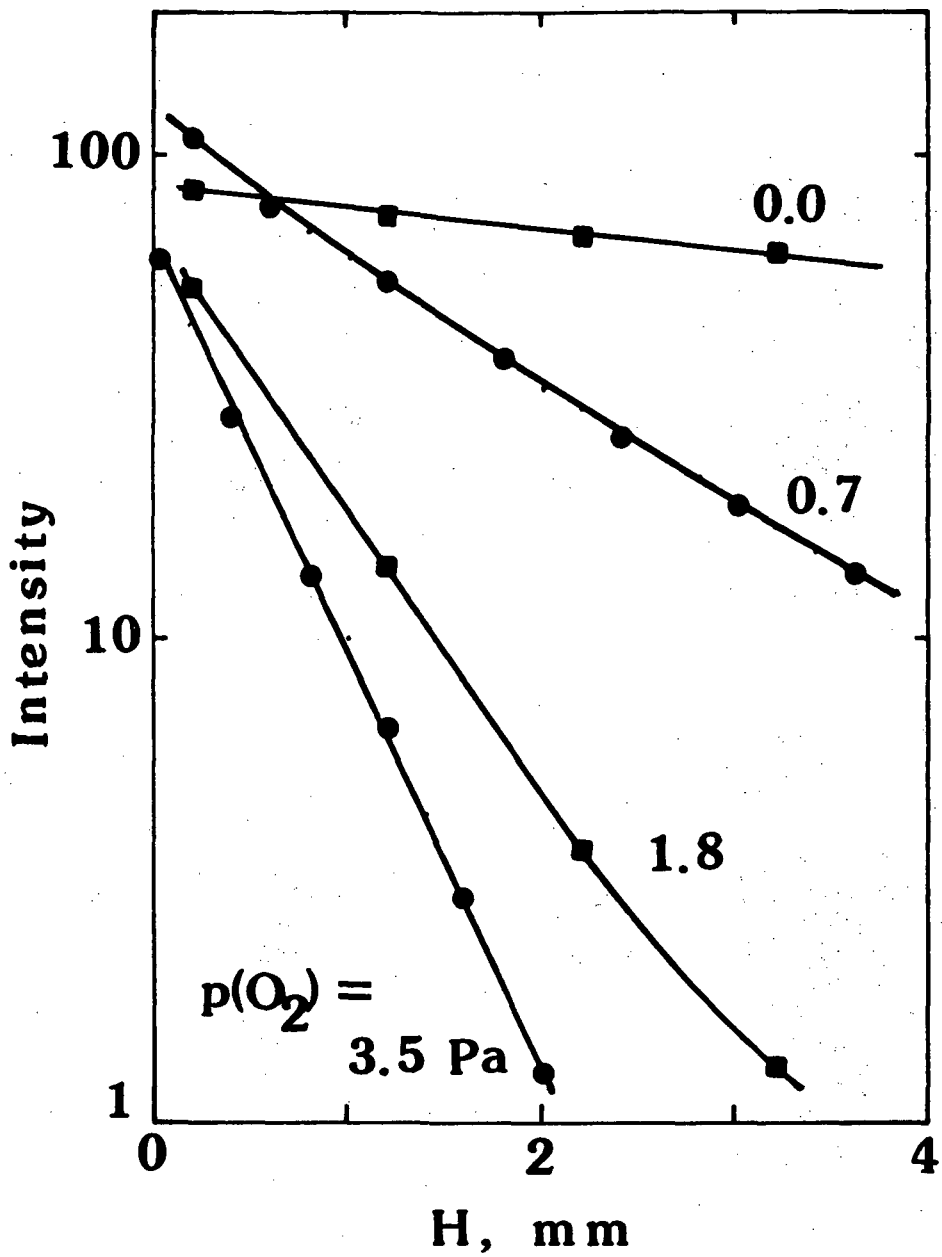


Figure 13 - Al-Atom Fluorescence Intensity versus Height Above a Levitated Sapphire Sphere.

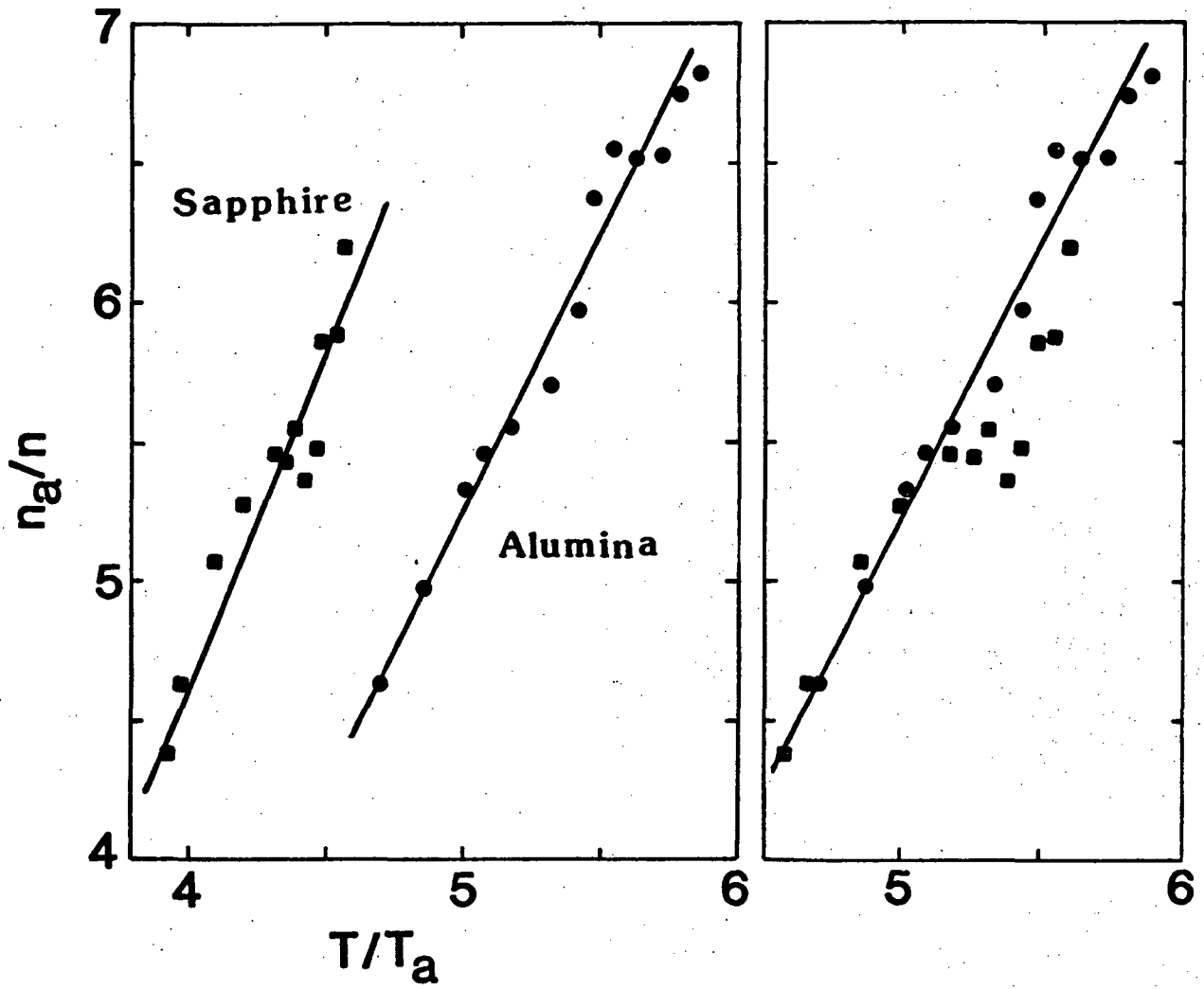


Figure 14 - Test of Hg-Atom Fluorescence Thermometry. Ambient to high temperature Hg-atom concentration ratio versus apparent specimen temperature to ambient temperature ratio. In the right hand panel, the sapphire data are plotted at temperature ratios adjusted according to the sapphire to alumina temperature corrections deduced from Al-atom fluorescence measurements over levitated sapphire and alumina spheres.

higher temperatures, according to the temperature corrections that are deduced from the Al-atom fluorescence data in Figure 10. The ambient temperatures were between 305 to 320K. It can be seen that the temperature adjusted sapphire data agree with the alumina data to about ±50K.

A small departure of the temperature adjusted sapphire data from the line drawn through the alumina data appears at temperature ratios greater than about 5.2. This error may arise from differences in the thermal diffusion effects for the two experiments. Alumina specimens require a greater laser power to achieve a given temperature than do sapphire specimens, and the apparatus achieves a greater ambient temperature for the alumina than for the sapphire experiments.

The precision of temperatures obtained by gas density thermometry was ca. ± 3% in these experiments, with sapphire and alumina specimens of nearly equal mass and diameter and under nearly identical levitation gas flow rates and ambient pressures. Large temperature gradients in the wake of levitated specimens, and small variations in the position of the specimen were major contributors to scatter of temperature measurements. Also, thermal diffusion effects influence the measured density ratios, by amounts that depend on the gas flow rates and ambient pressures, and the method would not be easily applied to other aerodynamic levitation experiments.

For containerless experiments in space, where negligible convective effects can be achieved in nonisothermal experiments, this method of gas density thermometry should provide accurate absolute temperature measurements. In space, reduced convection rates would yield smaller temperature gradients and allow gas density measurements whose precision exceeds that (±3%) achieved here.

4. Molybdenum evaporation: Figure 15 presents the intensity versus temperature data obtained on electromagnetically levitated molybdenum spheres. The plot of ln(IT) versus 1/T is chosen to present these results because intensity is proportional to atom number density, and IT is proportional to the Mo-atom pressure. If this proportionality is maintained, the vaporization enthalpy can be calculated from the slope of the plot:

$$d\ \ln(IT)/d(1/T) = -\Delta H^{o}_{T}/R \qquad (11)$$

At elevated temperatures, the concentration of Mo ($^7S_3$) atoms is sufficient that self-absorption of the fluorescent radiation reduces the measured intensity. The self-absorption effect is analyzed as follows.

The concentration of absorbing atoms is:

$$n_a = C_a \exp(-\Delta H^{o}_{T,a}/RT)/T \qquad (12)$$

and the concentration of atoms from which fluorescence is induced is:

$$n_f = C_f \exp(-\Delta H^{o}_{T,f}/RT)/T \qquad (13)$$

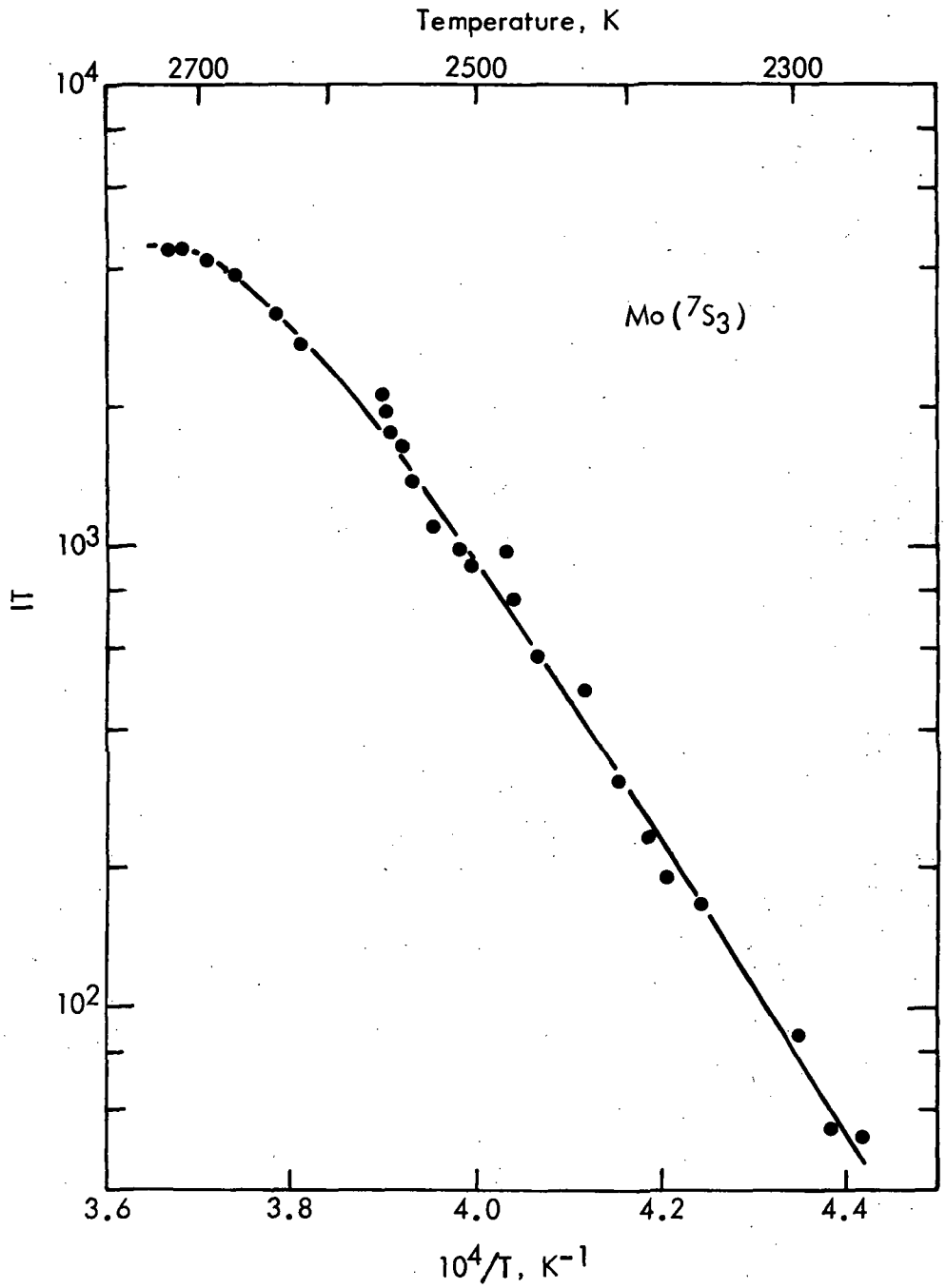


Figure 15 - Temperature Dependence of Mo ($^7S_3$) Ground State Fluorescent Intensity over Electromagnetically levitated, CW $CO_2$ Laser Heated Molybdenum Spheres, in Vacuum.

The fluorescence intensity produced, $I_0$, is reduced by the self-absorption effect to the measured intensity, I:

$$I/I_0 = \exp(-kn_a) \tag{14}$$

where the self-absorption coefficient, k, has been assumed constant over the relatively small temperature range in which this analysis of self-absorption will be applied. We also neglect the small variation of evaporation enthalpy and entropy over the temperature range of the experiment by assuming that $\Delta H^o_{T,a}$ and $\Delta H^o_{T,f}$ are independent of temperature. $I_0$ is proportional to $n_f$, and we obtain:

$$\ln IT = A + B/T + C \exp(B'/T)/T \tag{15}$$

where $B = -\Delta H^o_{T,f}/R$ and $B' = -\Delta H^o_{T,a}/R$. In the present case, B and B' are equal, and an iterative least squares analysis of the data yields the constants, A, B, and C. For the more general case, where fluorescence occurs into an energy level that differs from the one excited by the laser, the difference between B and B' is calculated from the known energy difference of the two levels.

Analysis of the molybdenum data gives $\Delta H^o_{2500} = 613 \pm 15$ kJ/g-mole and the line drawn through the data in the figure. Similar experiments with tungsten evaporation show that the self-absorption effect is accurately modeled if $I/I_0 > 0.5$. Data that do not meet this test have not been used in the data reduction procedure.

The expected evaporation enthalpy differs from that listed in tables[5,9] of thermodynamic properties ($\Delta H^o_{2500} = 633.5$ kJ/g-mole), which pertains to evaporation into an equilibrium distribution of atomic electronic states. The experiment studied evaporation into a single electronic state:

$$Mo(s) = Mo(^7S_3) \tag{16}$$

for which accepted thermodynamic data[5,9] yield $\Delta H^o_{2500} = 633 \pm 2$ kJ/g-mole. (The difference between this and the equilibrium enthalpy of evaporation is small because molybdenum atoms display no low lying electronic states.[13])

The temperature range of the Mo vaporization study was 2260 to 2730K. The true specimen temperatures were measured with a calibrated optical pyrometer, and corrected for the known[14] temperature dependent emittance of Mo. If the pyrometer calibration error were +7K at 2260K and -7K at 2730K, the measured value of $\Delta H^o_{2500}$ would agree with the literature value. Such corrections are slightly outside the uncertainties in the pyrometer calibration (against a pyrometer that was calibrated at the National Bureau of Standards). However, the precision of our enthalpy measurement, which does not include uncertainty in the pyrometer calibration, and the pyrometer calibration uncertainty easily account for the difference between the measured and literature values for Mo evaporation to the atomic $^7S_3$ state.

5. Tungsten evaporation: Preliminary tungsten evaporation results were presented in our first annual report.[1] At the time of that report, the departure of ln(IT) versus 1/T plots from a straight line at higher temperatures had not been identified as a self-absorption effect.

Most of the electronic transitions that have been laser pumped are shown as solid lines in Figure 16. Others can be identified from the list of wavelengths in Table 2, and tables of tungsten spectra.[7] Fluorescence was collected at the pumping wavelength or from the transitions indicated by dashed lines in the figure. Intensity versus temperature data were obtained for six electronic states.

Discrimination against scattered laser radiation was achieved by delayed detection at the exciting wavelength or by monitoring fluorescence at a wavelength different from that of the laser. Delayed detection was not possible for the smallest intensities when a detection time constant ca. 2 μs was employed. Then good scattered light rejection was achieved if the light trap opposite the window through which fluorescence was collected was kept clean.

Figure 17 presents intensity versus temperature data for tungsten atoms in the $^5D_1$ state at three different argon pressures. LIF from the $^5F_2^0$ state was used in these experiments. Sensitivity is greater at the higher pressure because the tungsten atoms diffuse less rapidly. The concentration in the immediate wake of the filament, where LIF was produced, is then larger. The reduction in self-absorption effects at lower pressures is much greater than can be explained by reduced concentration-distance product in the region that fluorescence must pass through. At low pressures, the W-atom mean free path is about equal to the distance from the filament to the point of LIF. Then, the velocity vectors of the atoms detected differ from those of the absorbing atoms, and the self-absorption effects are reduced by the doppler shift between the fluorescence and absorption lines.

Figure 18 presents results for five metastable electronic states. (All levels below the $^7F^o$ states are even levels, for which the sum of electron angular momentum quantum numbers is even, and are metastable.)

The term diagram (Figure 16) shows that fluorescence detection of $^3P_0$ and $^5D_0$ atoms can be achieved by use of common upper level at $E = 34{,}342\ cm^{-1}$. In a single experiment, fluorescence from the 34,342 $cm^{-1}$ to the $^5D_0$ state was used to measure $^3P_0$ and $^5D_0$ concentrations. No change in the experimental geometry occurred between the two sets of intensity measurements and nearly identical self-absorption effects should thus be obtained. The intensity ratios would then be free from self-absorption effects. Figure 19 presents the results, with the $^3P_0$:$^5D_0$ intensity ratios plotted at the bottom of the figure. The expected absence of self-absorption effects on the intensity ratios is obtained. The $^5D_0$ to $^3P_0$ excitation energy derived from the slope of the ratio plot is 110 ± 13 kJ/g-mole, in good agreement with the spectroscopic value (114.0 kJ/g-mole) for this energy.

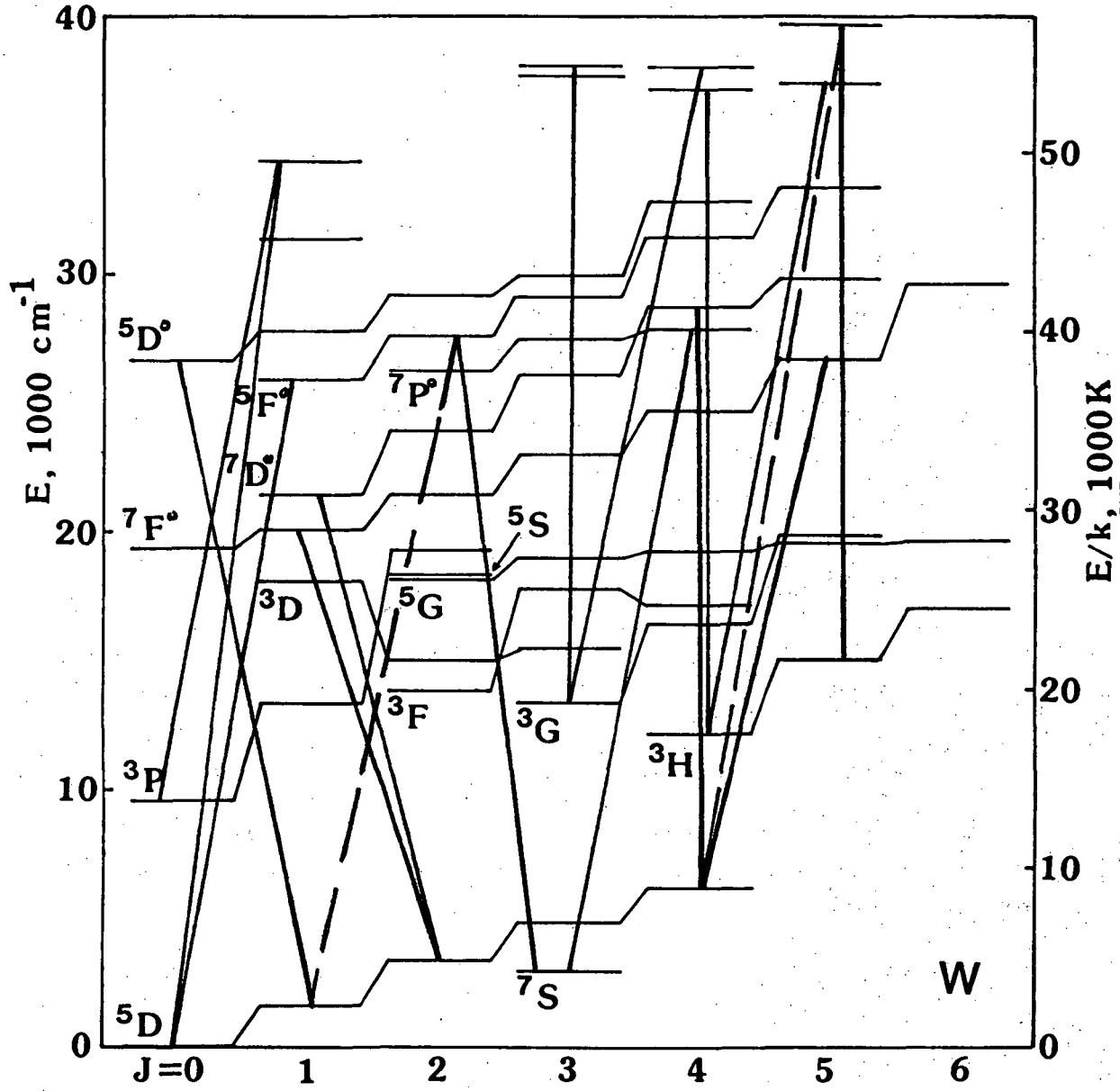


Figure 16 - Partial Energy Level Diagram for Atomic Tungsten. The solid lines indicate transitions that were laser pumped. The dashed lines are the transitions used to monitor fluorescence induced in $^7S_3$ and $^3H_5$ atoms.

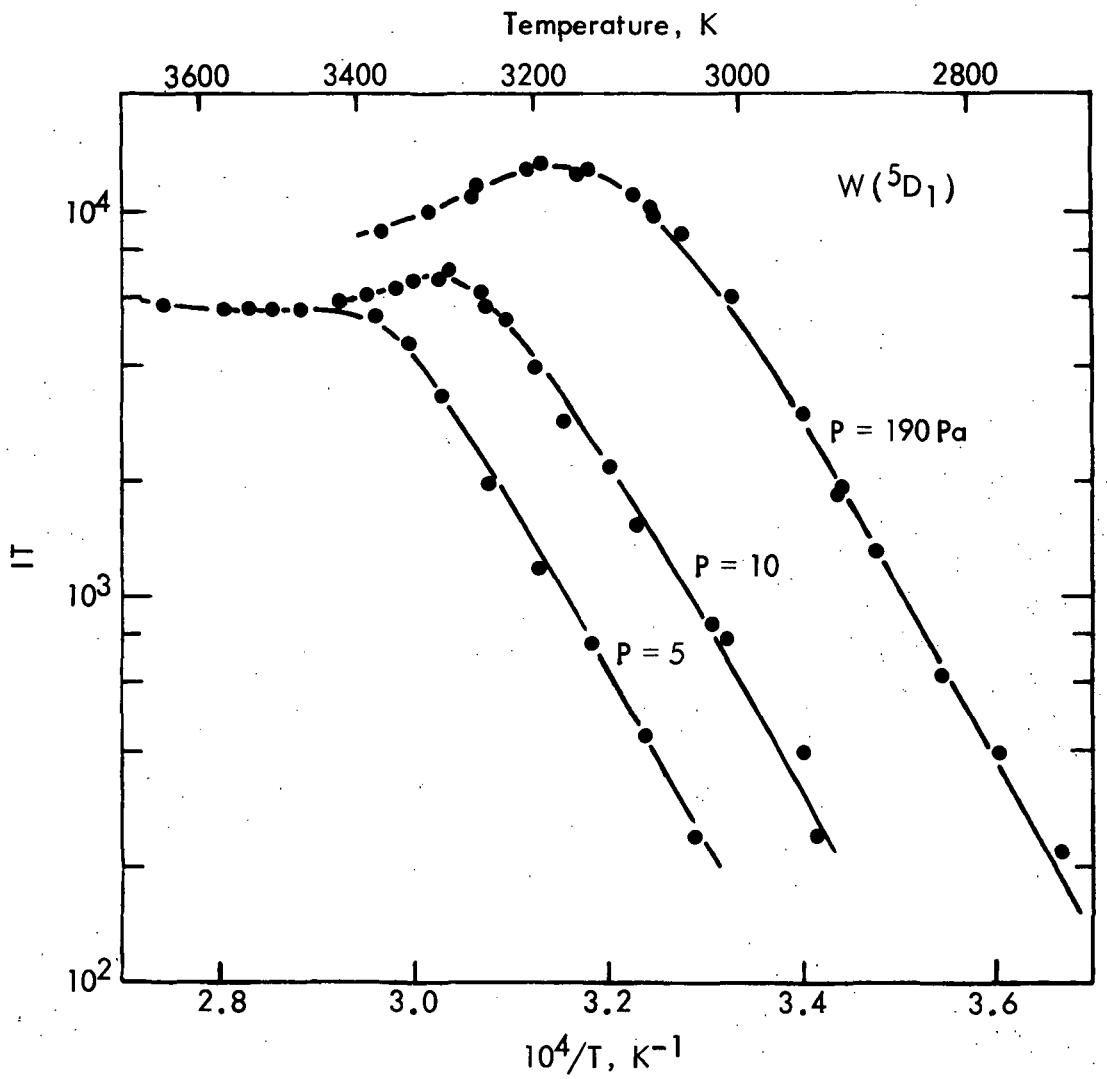


Figure 17 - Temperature Dependence of Fluorescence Intensity for $W^5D_1$ Ground State Atoms in the Wake of an Electrically Heated Tungsten Filament. Different pressures of flowing argon gas (velocity≈30 m/s) were used for the three experiments.

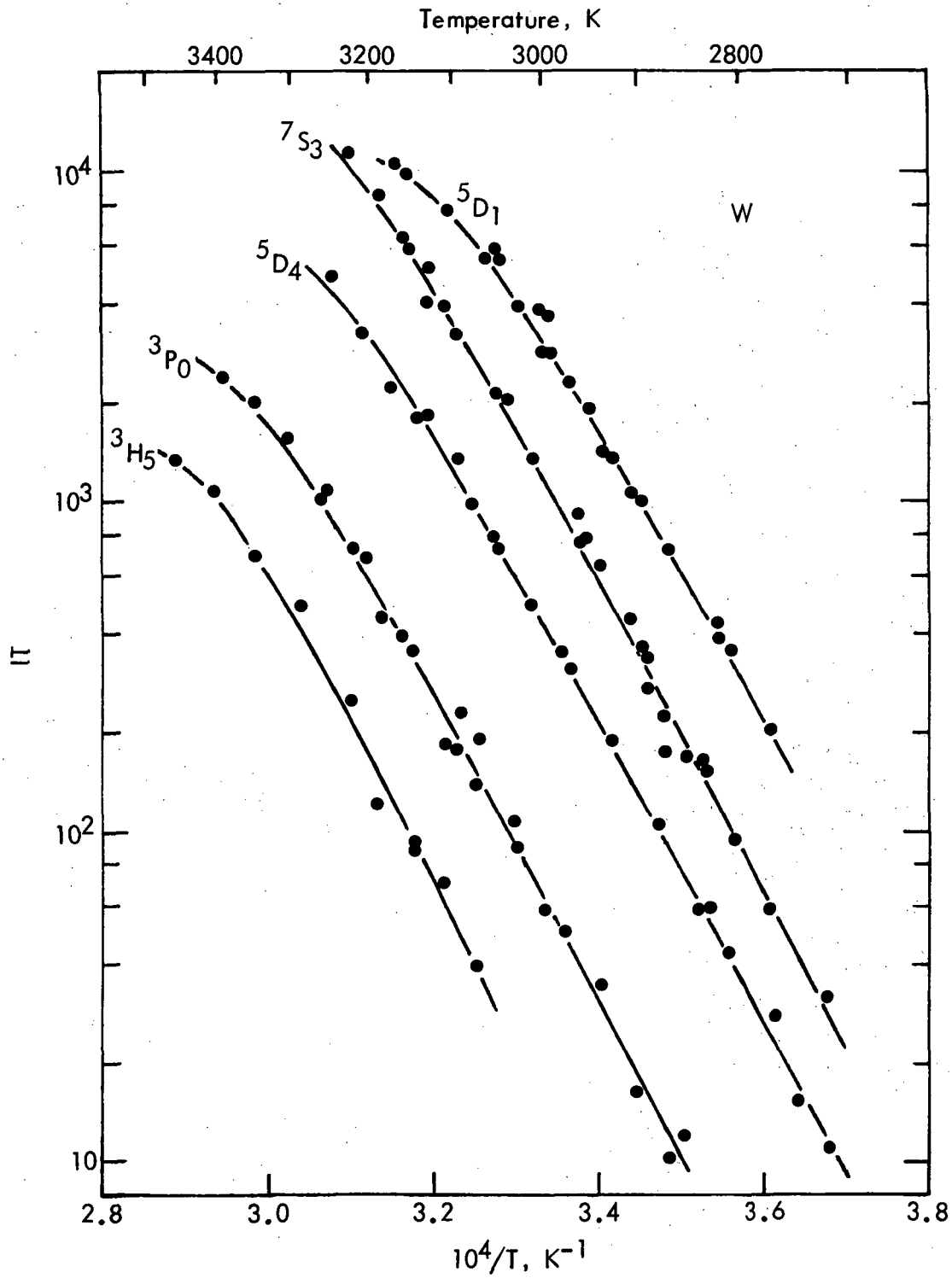


Figure 18 - Temperature Dependence of Fluorescent Intensity for Five Electronic States of Atomic Tungsten in the Wake of Electrically Heated Tungsten Filaments. The argon flow velocity was about 30 m/s at p = 190 Pa.

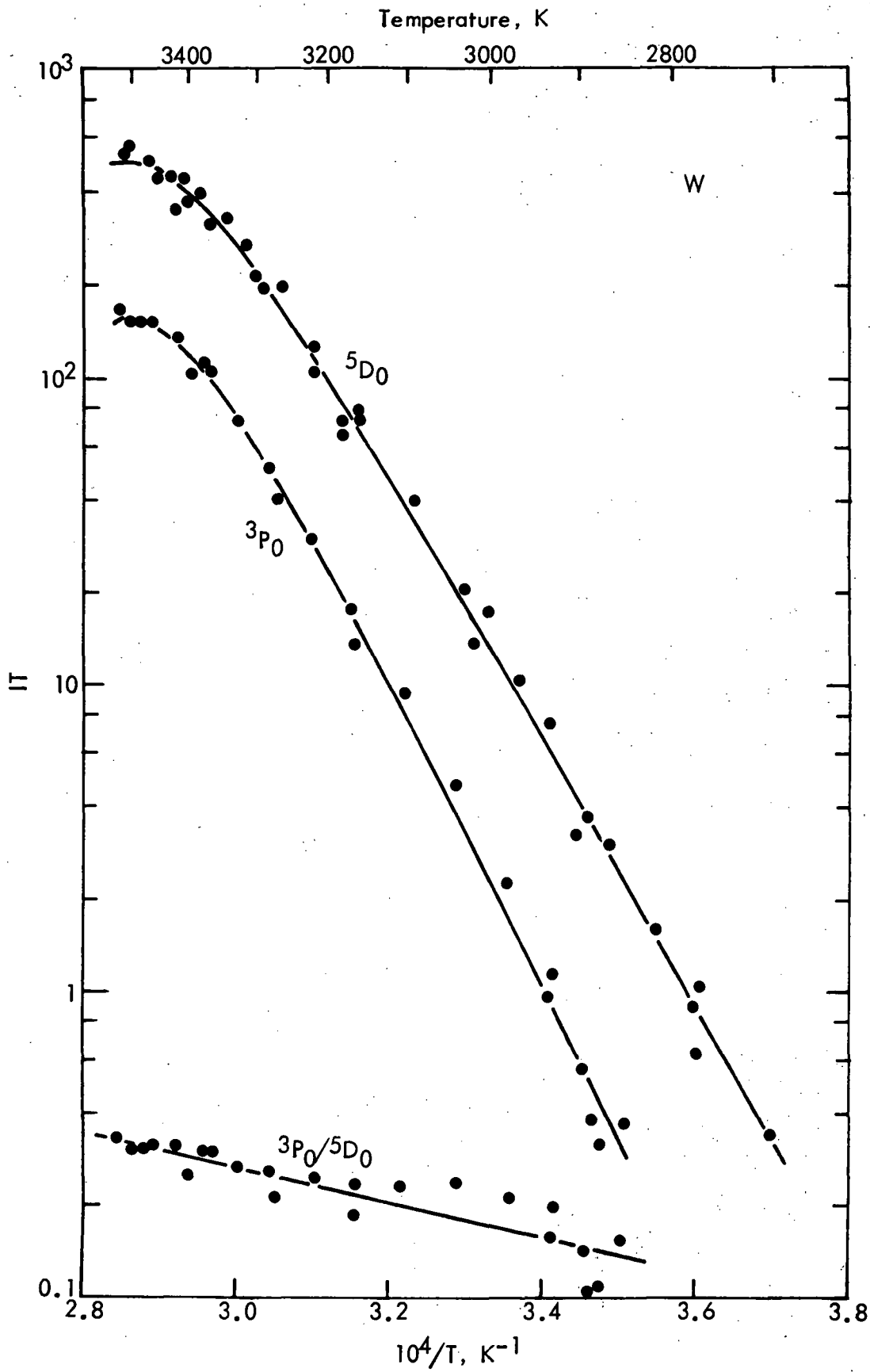


Figure 19 - Measurement of the $^3P_0:^5D_0$ Fluorescence Intensity Ratio. Both states were excited to the E = 34,342 $cm^{-1}$ electronic state and fluorescence into the $^5D_0$ state was observed at $\lambda$ = 291.1 nm. Self absorption effects occur at high temperatures but do not influence the calculated intensity ratios.

Table 4 presents the enthalpies of evaporation calculated from the several experiments at p = 190 Pa. The table lists the metastable electronic state that was studied, its electronic excitation energy, and the enthalpy of tungsten evaporation into this state as calculated from Eq. (15). The difference between the evaporation enthalpy and the electronic excitation energy is the enthalpy of evaporation to ground state atoms, which is given in the last column. The average enthalpy of evaporation to the $^5D_0$ ground state at ($\bar{T}$ = 3070K) is 831 kJ/g-mole and the average deviation of the eight measurements is 21 kJ/g-mole. The literature value[5] for this quantity is 825 ± 4 kJ/g-mole. (The enthalpy of evaporation[5] to an equilibrium distribution of W-atom electronic states is 860 kJ/g-mole at 3070K.)

TABLE 4

TUNGSTEN FILAMENT EVAPORATION RESULTS

| Atomic State | Energy kJ/g-mole | Evaporation Enthalpies, kJ/g-mole: Measured State | Evaporation Enthalpies, kJ/g-mole: Ground State |
|---|---|---|---|
| $^5D_0$ | 0 | 830 | 830 |
| $^5D_1$ | 20 | 871 | 851 |
| $^5D_1$ | 20 | 865 | 845 |
| $^7S_3$ | 35 | 909 | 874 |
| $^5D_4$ | 74 | 871 | 797 |
| $^3P_0$ | 114 | 914 | 800 |
| $^3P_0$ | 114 | 951 | 837 |
| $^3H_5$ | 180 | 992 | 812 |
| | | Average Value | 831 |
| | | Average Deviation | 21 |
| | | Literature Value | 825 ± 4 |

The pyrometer was calibrated in the range of these experiments by observing the apparent melting temperatures of tungsten and molybdenum filaments, with a precision ca. ±10K. An additional error in the pyrometer calibration results from uncertainty in the melting point of W (3680 ± 20K)[9] and Mo (2890K[5] or 2892 ± 10K[9]). The difference between the measured and literature values for the enthalpy of tungsten evaporation is easily within the error that may result from pyrometer calibration uncertainty and the enthalpy measurement precision.

However, repeat measurements of the $^3P_0$ evaporation enthalpies differ by amounts larger than the statistical errors in the derived $\Delta H$ values. It is thus apparent that systematic errors between experiments are significant. One such error arises because the experiments are carried out in argon. The gas temperature and density in the wake of the filament differ

from the values at the filament. Thus, density at the point at which fluorescence was measured is not strictly proportional to the vapor density at the filament. This problem does not occur for vacuum evaporation experiments.

6. Radiative lifetimes and collisional energy transfer rates: The radiative lifetimes, $\tau_r$, of laser excited atoms may be derived from the fluorescence intensity versus time subsequent to the laser pulse. This is accomplished by measuring intensity versus the boxcar averager aperture delay time, t. The slope of ln(I) versus t equals $-1/\tau_r$.

Jitter in the time interval between the electronic sync pulse (used to trigger the boxcar averager) and the laser pulse interferes with accurate measurement of short radiative lifetimes. In most cases, only upper limits on $\tau_r$ were obtained for $\tau_r < 20$ ns. Careful adjustment of the nitrogen laser thyraton ballast voltage in a few experiments gave trigger jitter equal to a few nanoseconds, and accurate values of small radiative lifetimes.

The measurement of longer radiative lifetimes required higher specimen temperatures, because intensity is inversely proportional to $\tau_r$ if the detector time constant is small compared to $\tau_r$. The experiments with electrically heated tungsten filaments used a constant current power supply and temperature drift during the measurement was significant in experiments with longer lived states. Temperature versus time measurements adequate to correct the results for the temperature dependence of atom concentration were not always obtained. Sensitive measurement of intensity versus temperature for long lived radiating states was easily accomplished by using a detection time constant that measured the integrated fluorescent light output.

Table 5 presents radiative lifetime data for various electronic states of W, Mo, B, and La. Laser trigger jitter was minimized for Mo, B, and La measurements. Temperature corrected data were obtained only for the W-atom $^7F_2^0$ and $^7D_1^0$ states in experiments for which the trigger jitter was about ±150 ns.

TABLE 5

MEASURED AND LITERATURE VALUES FOR THE RADIATIVE LIFETIMES OF B, Mo, La, AND W ATOMS

| Element | Term Symbol | Excitation Energy, $cm^{-1}$ | Radiative Lifetime, ns |
|---|---|---|---|
| B | $^2S_{1/2}$ | 40,040 | 6.2<br>(5.1 ± 25%)[19,20] |
| Mo | $^7P_4^0$ | 26,320 | 19 ± 5<br>(14.7)[29] |

TABLE 5 (continued)

| Element | Term Symbol | Excitation Energy, $cm^{-1}$ | Radiative Lifetime, ns |
|---|---|---|---|
| La | | 20,019 | 13 ± 3 |
| W | $^7F_1^o$ | 20,064 | 1,500 ± 500 |
| | $^7F_2^o$ | 21,449 | 810 - 1,140 |
| | $^7D_1^o$ | 21,454 | 260 - 810 |
| | $^7F_5^o$ | 26,676 | 700 ± 300 |
| | $^5F_2^o$ | 27,663 | < 20 |
| | $^5D_1^o$ | 27,778 | < 10 |
| | $^7P_4^o$ | 27,890 | < 20 |
| | $^5F_4^o$ | 31,433 | < 20 |
| | | 34,342 | 90 ± 30 |
| | | 37,146 | < 20 |
| | | 37,309 | < 20 |
| | | 39,183 | < 10 |
| | | 42,450 | < 10 |

It can be seen that the energy separation of the W-atom $^7F_2^o$ and $^7D_1^o$ states is only 5 $cm^{-1}$. Energy transfer between these states is caused by collision with argon atoms. A term diagram showing the processes observed in our study of $^7F_2^o$ and $^7D_1^o$ fluorescence is given in Figure 20. Laser excitation from the $^5D_1$ state was used, and fluorescence from both upper levels was observed at 466 and 505 nm. The term diagram indicates collisional energy transfer between the two excited states.

Intensity versus delay time data at $\lambda$ = 466 and 505 nm after laser excitation of these two states were obtained at an ambient pressure equal to 73 Pa and are given in Figure 21. It can be seen that emissions from the $^7D_1^o$ state initially increases with delay time after laser excitation of the $^7F_2^o$ state due to the energy transfer process.

Analysis of the data in Figure 21 proceeds as follows. Let $A_1$, $A_2$, and KP be the rate constants for radiation from the $^7D_1^o$ (state 1) or $^7F_2^o$ (state 2) atoms, and for collisional energy transfer from state 2 to state 1. The rate constant for the reverse process is 5/3 KP. Then, the excited atom concentrations vary with time as:

$$dn_1/dt = -A_1\, n_1 + KP(n_2 - 5/3\, n_1) \qquad (17)$$

$$dn_2/dt = -A_2\, n_2 - KP(n_2 - 5/3\, n_1) \qquad (18)$$

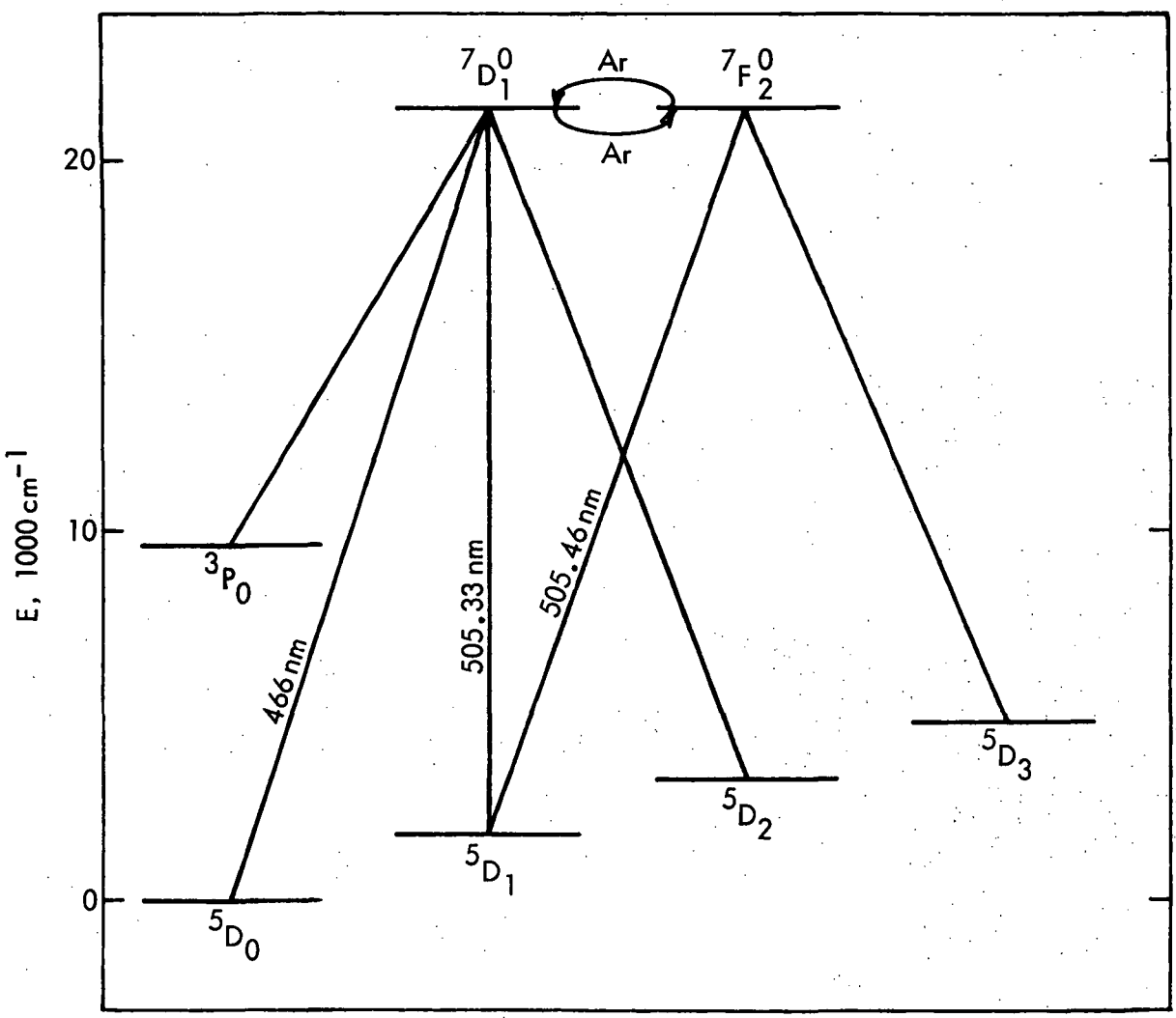


Figure 20 - Transitions of Tungsten $^7D_1^o$ and $^7F_2^o$ Atoms.

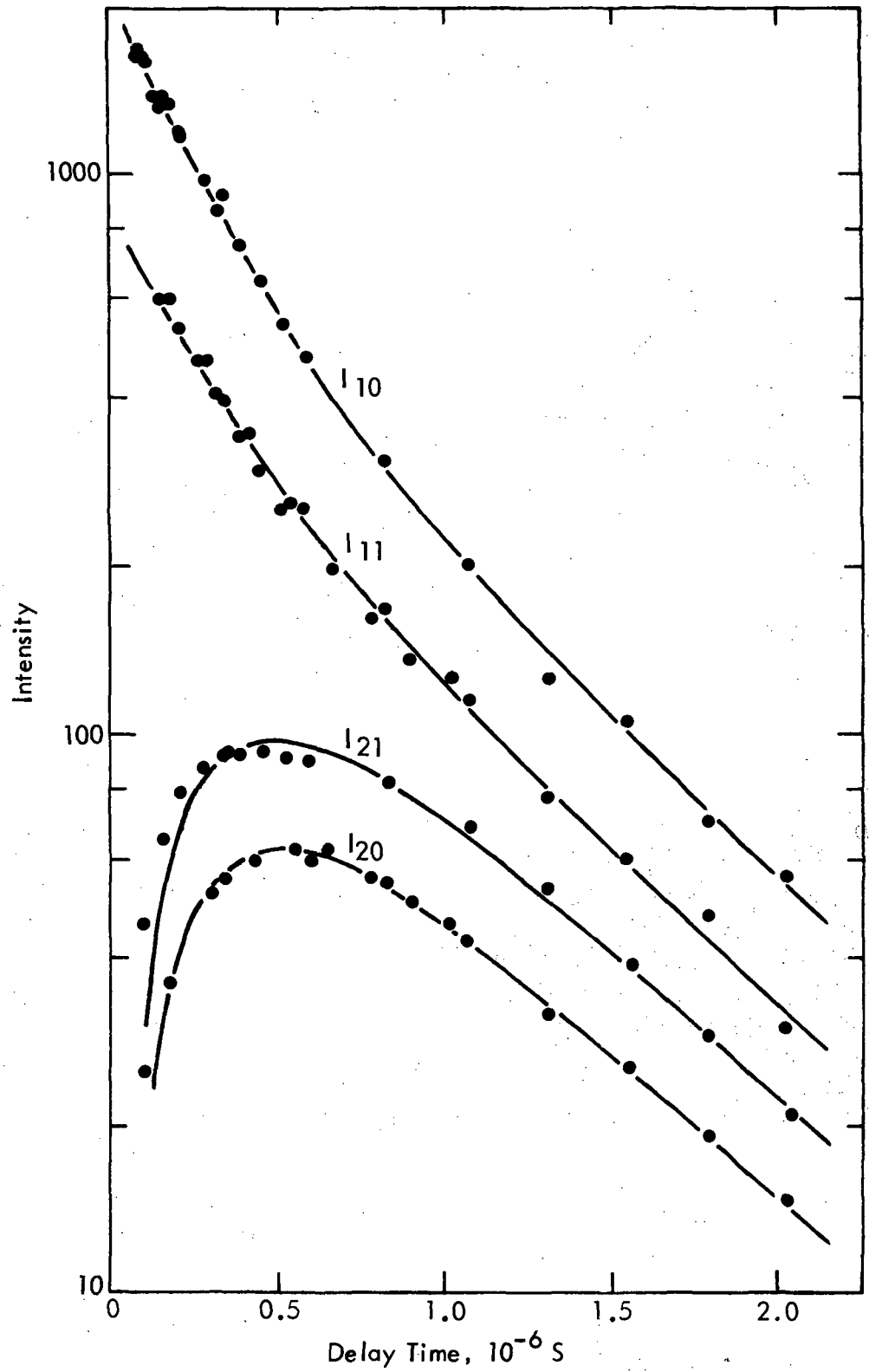


Figure 21 - LIF Intensity versus Delay Time for Emission by Tungsten $^7D_1^o$ and $^7F_2^o$ Atoms. $I_{ij}$ denotes laser excitation of $^7D_1^o$ (i=1) or $^7F_2^o$ (i=2) and emission to $^5D_0$ (j=0) at $\lambda$ = 466 nm or to $^5D_1$ (j=1) at $\lambda$ = 505 nm. The 505 nm emissions from the two upper levels were not resolved.

The solution of these equations is:

$$n_i = C_i \exp[-B_1(t - t_0)] + D_i \exp[-B_2(t - t_0)] \quad (19)$$

where $B_1$ and $B_2$ are equal for both species but $C_i$ and $D_i$ depend on the state that is excited by the laser.

Let subscript j = 0 denote the 466 nm emission from $^7D_1^0$ to $^5D_0$ and j = 1 the 505 nm emissions from $^7D_1^0$ and $^7F_2^0$ to $^5D_1$. Let subscript i = 1 or 2 denote laser excitation of the $^7D_1^0$ or $^7F_2^0$ states. Then:

$$I_{ij} = C_{ij} \exp[-B_1 (t - t_0)] + D_{ij} \exp[-B_2 (t - t_0)] \quad (20)$$

The lines drawn through the data in Figure 21 are a best fit of the data to these equations, which gave:

$$\begin{aligned} t_0 &= 61 \text{ ns} \\ B_1 &= 1.23 \text{ E6/sec} \\ B_2 &= 3.81 \text{ E6/sec} \\ C_{10} &= 588 \\ C_{20} &= 159 \\ C_{11} &= 352 \\ C_{21} &= 242 \\ D_{10} &= 1{,}177 \\ D_{20} &= -159 \\ D_{11} &= 378 \\ D_{21} &= -233 \end{aligned} \quad (21)$$

The equation:

$$C_{20} = -D_{20} \quad (22)$$

was used to obtain the value of $t_0$ derived above.

The values of $B_1$ and $B_2$ are related to $A_1$, $A_2$, and KP by:

$$B_1 + B_1 = A_1 + A_2 + 8/3 \text{ KP} \quad (23)$$

$$B_1 B_2 = A_1 A_2 + \text{KP}(A_1 + 5/3 \text{ KP}) \quad (24)$$

These are two equations in the three unknowns. Therefore, the results only give values of $A_1$ and $A_2$ versus KP. With $A_1 > A_2$ we obtain:

$$\begin{aligned} 1.23 &< A_1 < 3.81 \text{ E6/sec} \\ 0.88 &< A_2 < 1.23 \text{ E6/sec} \\ 0 &< \text{KP} < 0.97 \text{ E6/sec} \end{aligned} \quad (25)$$

A value of 1.0 E6/sec for KP is equivalent to a cross-section for collisional energy transfer approximately 2E-15 $cm^2$.

It would be possible to extend this analysis by obtaining measurements at a different pressure, or considering the ratios $C_{ij}/D_{ij}$ which depend on $A_1$, $A_2$, and KP. However, Figure 20 shows systematic deviations in the fit of Eq. (20) to the data at small delay time intervals. This systematic difference between theory and experiment is in part due to jitter in the laser trigger. Data obtained at reduced laser trigger jitter should be obtained before attempting to improve on the limits expressed by Eq. (25).

Two facts make energy transfer a significant process in fluorescence from the $^7F_1^0$ and $^7D_2^0$ states. First, these states have large radiative lifetimes. Second, their energy separation is very small. This combination of properties does not exist for other transitions that were studied.

7. <u>$LaB_6$ evaporation</u>: Evaporation of aerodynamically levitated and laser heated $LaB_6$ spheres was investigated by measuring B and La-atom LIF in the wake of the levitated specimen. Spatially resolved LIF data were obtained for boron atoms and intensity versus temperature experiments were obtained for boron and lanthanum. Absolute specimen temperatures were calculated by using the known spectral emittance[15] of $LaB_6$.

LIF data were obtained for boron atoms over $LaB_6$ by exciting the $^2P_{3/2}^0$ to $^2S_{1/2}$ transition at 249.8 nm and observing the unresolved emission of $^2S_{1/2}$ atoms to the $^2P_{1/2}^0$ and $^2P_{3/2}^0$ states. La-atom LIF was observed at 527.1 nm after laser excitation of the 20,019 $cm^{-1}$ state from the ground state at 499.39 nm.

Figure 22 presents intensity versus temperature data for three boron-atom data sets and one set of data for lanthanum. Data set B-1 was obtained with a 400-μ detector aperture. A 50-μ detector aperture was used for the other data sets. Curvature in the log(I) versus 1/T plots results from saturation of the photomultiplier output in data set B-1. Photomultiplier saturation was avoided by use of the smaller detector aperture for the remaining experiments. Curvature of the line drawn through data sets B-2 and B-3 is attributed to self-absorption of fluorescence, which increases with temperature. The self-absorption effect is measured as the departure of the measured LIF intensities from an extrapolation of the lower temperature data. The lines drawn through boron atom data sets B-2 and B-3 were obtained from an analysis of the self-absorption effect that is described later.

The self-absorption coefficient for La-atom LIF is small compared to that for B-atom LIF, because (a) the La-atom transition strength is small compared to that for boron; (b) La-atom emission is split into several resolved hyperfine components;[16,17] and (c) the La-atom concentration over $LaB_6$ is smaller than the B-atom concentration. The La:B transition strength is smaller than the inverse radiative lifetime ratio (~ 6:13), because the lanthanum emission occurs to several lower states. The curve drawn through the La data has the same shape as that derived for data set B-2. This curve was fit to the La-2 data by making a change of 2.5E-5 $K^{-1}$ in the 1/T axis and an appropriate change in the intensity. This change in the 1/T axis indicates the effective La:B self-absorption coefficient ratio is about 0.4.

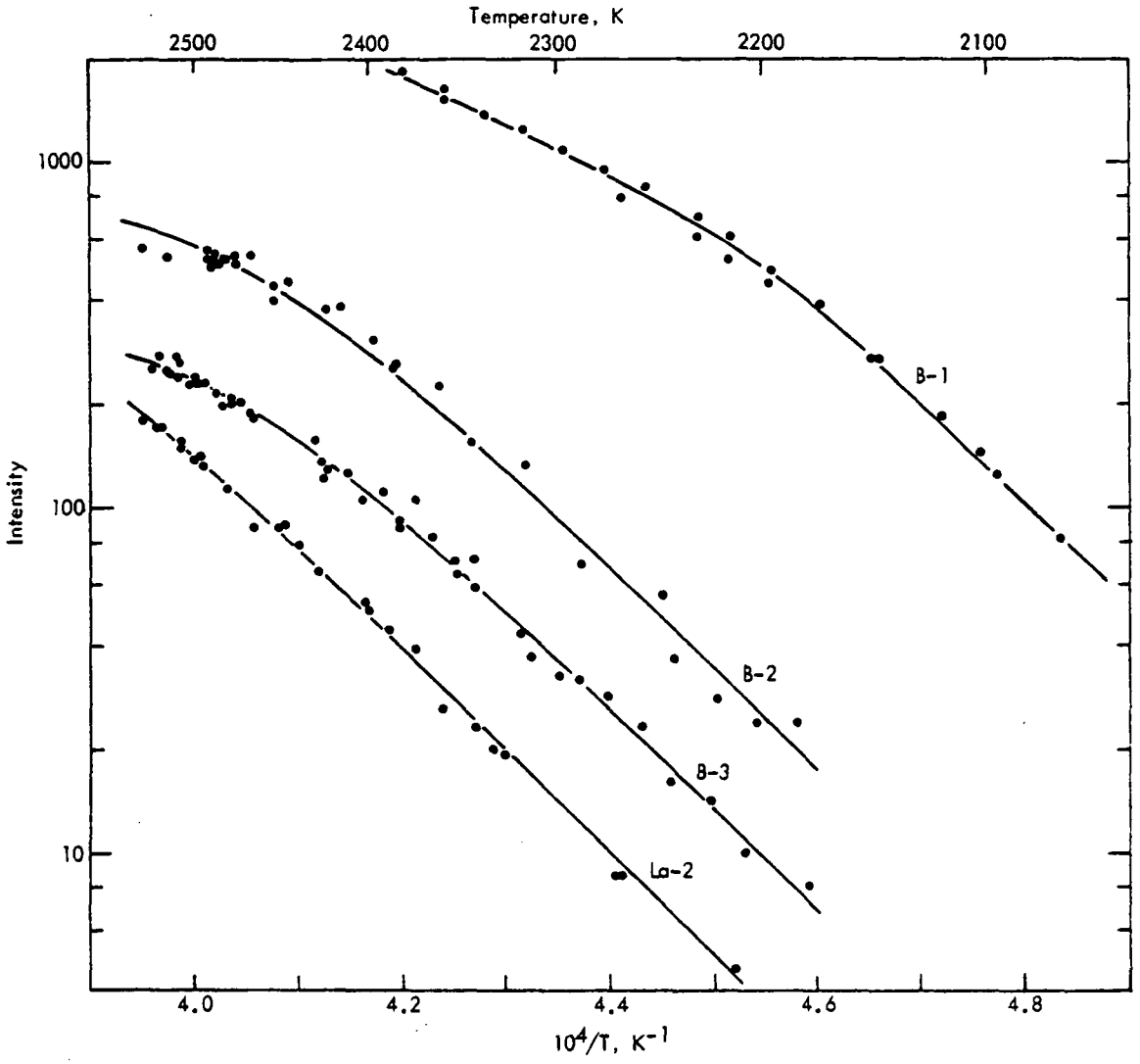


Figure 22 - Temperature Dependence of Boron and Lanthanum LIF Intensities over an Aerodynamically Levitated and CW $CO_2$ Laser Heated 0.28 cm Diameter $LaB_6$ Sphere. A smaller fraction of the LIF was collected in experiments B-2, La-2, and B-3 to eliminate overload of the photomultiplier detector that was observed at high intensities in experiment B-1. The ambient argon pressure was 29.6 to 30.6 torr. The intensities plotted for experiments B-2 and La-2 are 4 and 0.5 times the measured intensities respectively.

At temperatures above about 2300K, spatial variations in the boron atom concentrations cannot be equated to spatial variations in the LIF intensity because self-absorption will also be position dependent. Measurements of the axial and radial variation of the B-atom LIF intensity at temperatures where self-absorption was negligible gave the results in Figures 23 and 24. Figure 23 plots the axial variation of B-atom concentration with distance from the specimen surface in the wake of the specimen. Figure 24 plots the radial variation in the B-atom concentration at the wake distance for which I(T) data were measured. The arrows in each figure mark the point from which LIF data were measured.

Absolute concentrations may be calculated from the data in Figures 22 through 24 and the known strengths of the self-absorbing transitions. To do so, it is necessary to assume a relation between the measured spatial variations in B-atom concentration and the spatial variation of temperature, so that the calculation can account for variable Dopper spreading of the self-absorption lines. We take the gas temperature, $T_g$, and the specimen temperature, $T_s$, to be equal at the specimen surface and relate gas temperature to the ambient temperature, $T_a$, and the measured boron concentrations by the equation:

$$(n/n_s) = (T_s/T)[(T - T_a)/(T_s - T_a)]^{\beta} \qquad (26)$$

where the local B-atom concentration is n and that at the specimen surface is $n_s$. Values of the exponent, $\beta$, are given by a model that is described elsewhere.[22] These values depend on the ratio of the thermal diffusivity of argon to the binary boron/argon diffusivity and on the thermal diffusion coefficient for boron in argon. We obtained $\beta = 1.01$ for $1{,}000K < T < T_s$ and $\beta = 0.91$ for $T < T_s < 1{,}000K$.

If temperature and concentration were uniform in the self-absorbing interval, $0\text{-}\ell$, the measured intensity would be reduced by the factor $f = \exp(-\overline{k\ell})$ due to self-absorption effects. This factor is given by Mitchell and Zemansky[18] as:

$$f = \exp(-\overline{k\ell}) = \int_{-\infty}^{\infty} \exp(-\omega^2)\exp(-k_o N\ell e^{-\omega^2})d\omega / \int_{-\infty}^{\infty} \exp(-\omega^2)d\omega \qquad (27)$$

where: $$\omega^2 = 4 \ln 2 \, (\nu - \nu_0)^2/\gamma^2 \qquad (28)$$

$$k_0 = (2/\gamma) \sqrt{\ln 2/\pi}(\lambda^2/8\pi)(g_2/g_1)A_{21} \qquad (29)$$

$$\gamma = (2\nu_0/c) \sqrt{2RT\ln 2/M} \qquad (30)$$

These equations integrate the self-absorption effect over the frequencies, $\nu$, of the line whose central frequency is $\nu_0$ and Doppler half-width, $\gamma$. The wavelength is $\lambda$ and the upper and lower state multiplicities are $g_1$ and $g_2$, respectively. $A_{21}$ is the probability per unit time for the radiative transition, equal to[19,20] 1.3E8/sec and 0.65E8/sec for the $^2S_{1/2} - {}^2P^0_{3/2,1/2}$ transitions, respectively. N is the concentration of atoms in the self-absorbing state. The temperature is T; R and M are the ideal gas constant and the molecular weight of boron; and c is the speed of light.

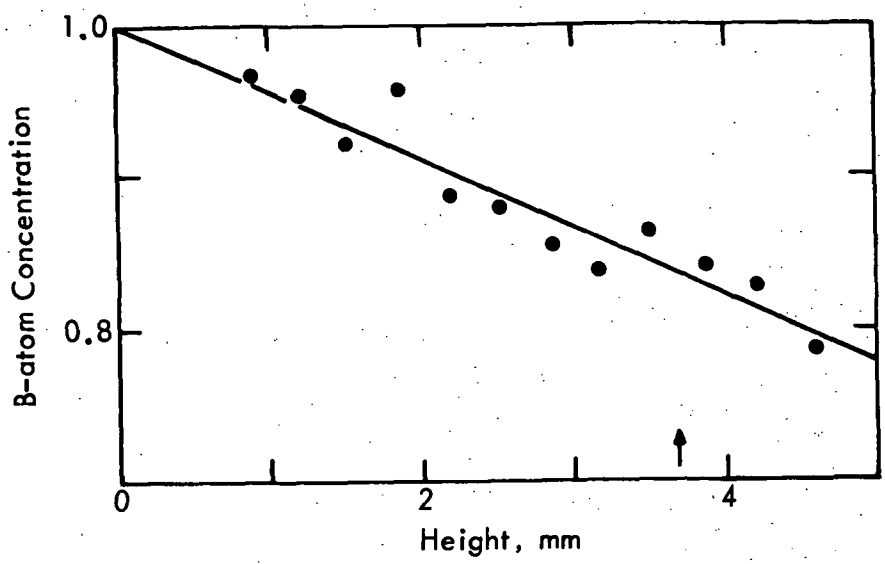


Figure 23 - Axial Boron-Atom Concentration Gradient in the Wake of a Levitated $LaB_6$ Sphere. Conditions were T = 2153K and p = 32 torr. LIF I(T) data were obtained at the location marked by an arrow.

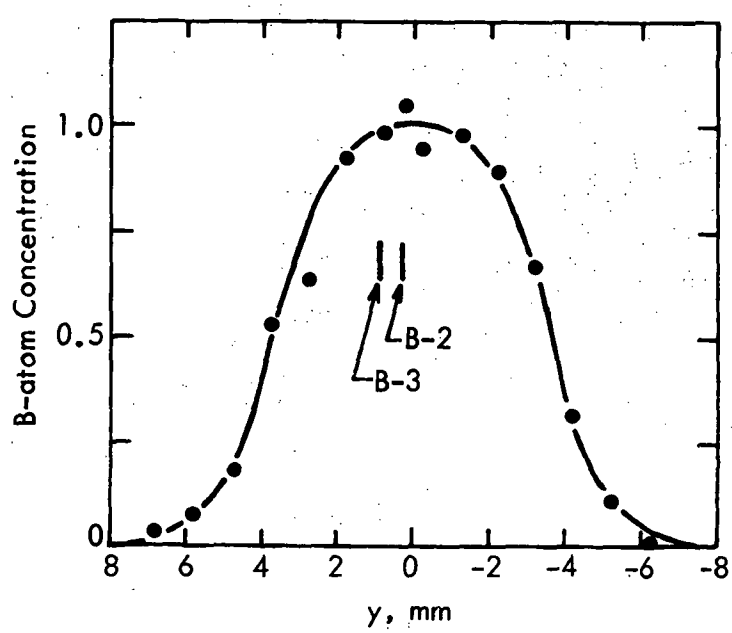


Figure 24 - Radial Variation of Boron-Atom Concentration. Data were obtained at the axial location marked in Figure 23 and at T = 2220K, p = 30.5 torr. The laser position is marked for LIF I(T) experiments. The light collected was emitted in the direction of the positive y-axis.

Extension of the above equations to the present case where temperature and concentration are not uniform gives:

$$f = \exp(-\overline{k\ell}) = \int_{-\infty}^{\infty} \exp(-\omega_e^2) \exp\{-k_{oe} N_e \int_0^{\ell} (T_e/T)^{1/2} (N/N_e)$$
$$\exp[-\omega_e^2(T_e/T)]d\ell\}d\omega_e / \int_{-\infty}^{\infty} \exp(-\omega^2{}_e)d\omega_e \quad (31)$$

where subscript e denotes values calculated at the position from which fluorescence is emitted. It is not necessary to include the small variation of $\lambda$ and therefore $k_{oe}$ with $\nu$ to obtain an accurate result from this equation.

The measured self-absorption effect allows absolute calibration of the intensity measurements and derivation of the equilibrium vapor pressure versus temperature relation. But the measured self-absorption effect depends on the equation used to extrapolate lower temperature I(T) data. Therefore, an iterative procedure was used to achieve simultaneous calibration of the intensity measurements and calculation of thermodynamic properties for the vaporization reaction.

The vaporization reaction is:

$$1/7\ LaB_6(s) = 1/7\ La(g) + 6/7\ B(g) \quad (32)$$

and the vapor pressure is given by:[21]

$$-RT \ln [p_{La}^{1/7}\ p_B^{6/7}] = \Delta H_{298}^0 + T\ \Delta fef \quad (33)$$

where $\Delta H_{298}^0$ is the enthalpy to be calculated for Reaction 32 and $\Delta fef = \Delta(G_T^0 - H_{298}^0)/T$ is available from thermodynamic property tables.[5,22]

Congruent evaporation of $LaB_6$ requires that the B:La flux ratio be 6:1. We estimate[22] that the effective B:La diffusion coefficient ratio is 1.88 to obtain $p_{La}/p_B = 0.313$. Then:

$$-RT \ln [0.313^{1/7}\ p_B] = \Delta H_{298}^0 + T\ \Delta fef \quad (34)$$

The equilibrium B-atom vapor pressure can be written:

$$p_B = C\ I\ T_s/(f''f'f) \quad (35)$$

C is a calibration constant, I is the measured intensity, and f' is the ratio of the B-atom concentration at the measurement point to that at the specimen surface (see Figure 23). The quantity f" accounts for evaporation kinetic effects. It equals the vapor pressure developed at the specimen surface divided by the equilibrium vapor pressure over $LaB_6$. The value determined[22] for this factor was 0.99. Then:

$$-RT\ \{\ln[0.313^{1/7}] + \ln[IT/(f''f'f)] + \Delta fef/R\} = \Delta H_{298}^0 + RT \ln C \quad (36)$$

The preceding equations were solved by the following iterative procedure:

1. Choose a trial value for $\Delta H^{o}_{298}$ and calculate $p_B$ for each data point from Eq. (34).

2. Calculate f for each data point from Eq. (31).

3. Calculate $\Delta H^{o}_{298}$ and ln C by a least squares fit of the data to Eq. (36).

4. Use the value of $\Delta H^{o}_{298}$ obtained in Step 3 to repeat Steps 1 through 3 until a constant value of $\Delta H^{o}_{298}$ is obtained.

The analysis described above gave the results presented in Table 6. The first two rows give the $LaB_6$ vaporization enthalpies calculated from data sets B-2 and B-3. These calculations used the nominal values, 0.49, for the evaporation coefficient, 5.1 ns for the boron atom $^2S_{\frac{1}{2}}$ radiative lifetime, and 1.88 for the B:La diffusivity ratio. The contributions of uncertain measurements of property values to the error in $\Delta H^{o}_{v,298}$ are also given in the table.

TABLE 6

STANDARD ENTHALPY FOR THE REACTION
$1/7\ LaB_6(s) = 1/7\ La(g) + 6/7\ B(g)$

| Data Set or Error Source | $\Delta H^{o}_{298}$ or Error (kJ/mol) |
|---|---|
| B-2 | 601.5 |
| B-3 | 604.3 |
| Error analysis: | |
| Temperature versus concentration function | ±1.0 |
| Evaporation kinetics | ±0.5 |
| Radiative lifetime of $^2S_{\frac{1}{2}}$ boron (±25%) | ±5.0 |
| Effective B:La diffusivity ratio (±14%) | ±0.4 |
| Temperature measurement (±8K) | ±2.0 |
| Standard deviation of average value | ±2.0 |
| Selected value | 602.9 |
| Estimated error | ±5.9 |

The selected value is the average result for the two experiments, $\Delta H^{o}_{v,298}$ = 602.9 ± 5.9 kJ/mol. This error was calculated by quadradic combination of the individual errors listed in the table.

Table 7 compares our result with values that may be calculated from the literature. The lanthanum sublimation enthalpy, 431 ± 4 kJ/mol selected by Hultgren et al.,[5] as well as solid $LaB_6$ and gaseous boron formation enthalpies from the indicated sources, were used to calculate the enthalpies for $LaB_6$ sublimation reported in the first four rows of the table. The present result (row 5) is consistent with the $LaB_6$ formation enthalpy reported by Topor and Kleppa[23] and the boron sublimation enthalpies selected by JANAF[24] or measured by Mar and Bedford.[25] It does not agree with the $LaB_6$ formation enthalpy reported by Storms and Mueller,[26,27] even when the calculation is based on larger values that have been reported[5,28] for the enthalpy of boron sublimation. (The $LaB_6$ result of Storms and Mueller is independent of the enthalpy of boron sublimation.)

TABLE 7

STANDARD ENTHALPY OF VAPORIZATION FOR 1/7 $LaB_6(s)$

| Source of Data for $LaB_6$; Boron | Enthalpy of Formation $LaB_6(s)$ | Enthalpy of Formation $B(g)$ | $\Delta H^\circ_{v,298}$ 1/7 $LaB_6(s)$ |
|---|---|---|---|
| Topor and Kleppa;[23] JANAF[24] | -400.4 ± 11.9 | 559.8 ± 12.6 | 598.6 ± 10.9 kJ/mol |
| Topor and Kleppa;[23] Mar and Bedford[25] | -400.4 ± 11.9 | 561.1 ± 3.3 | 599.7 ± 3.8 |
| Storms and Mueller[26,27] Hultgren et al.[5] | -254 ± 8 | 571.1 ± 2.1 | 587.4 ± 2.5 |
| Storms and Mueller[26-28] | -254 ± 8 | 574.9 ± 0.8 | 590.6 ± 1.5 |
| This research | | | 602.9 ± 5.9 |

## IV. DISCUSSION

The results obtained demonstrate several new methods by which LIF can be used for containerless high temperature property measurements and process control. Experience also indicates a number of improvements or changes that would be useful in earth- or space-based research. Accurate temperature measurement and control are critical requirements in such research, which cannot be satisfied by optical pyrometry if specimen emittances have not been independently measured or changed during an experiment or process.

1. Temperature measurement: Three new methods for temperature measurement can be evaluated on the basis of the current results. These methods use LIF measurements of gas density, atomic electronic state population ratios, or the velocities of evaporating atoms to determine temperature. The velocity measuring technique is applicable in vacuum and the gas density method requires an inert ambient atmosphere. The calculation of temperatures from electronic state population ratios or velocities requires the assumption that the gas is in thermal equilibrium with the hot surface of interest. The two techniques provide a check on this assumption because they would yield equal temperatures only by coincidence if the assumption was not correct.

Mercury is a convenient nonreactive, volatile seed gas for LIF gas density thermometry. However, thermal diffusion of Hg atoms in lighter gases has a large influence on the concentration gradients that develop in a nonisothermal gas. The rates of convective mass and heat transfer also influence temperature and concentration gradients, and the technique is therefore not easily applied in earth-based experiments. In space, convective effects can be avoided in containerless nonisothermal experiments and accurate calibration of Hg-atom LIF gas density thermometry may be achieved. Also, the smaller temperature gradients that obtain in the absence of convective heat transfer would allow a considerable improvement of the ±3% precision in temperature that was achieve in our experiments.

Accurate electronic state population ratios can be measured even when self absorption effects influence the relation between intensity and concentration (c.f., Figure 19). However, the precision of the ratios obtained in the current work is reduced by the need to calculate them from separate measurements of intensity versus temperature for the two species of interest. The precision of temperature measurement then influences the precision of the ratio measurements. For example, assume that the $^5D_0$ intensity versus temperature function is known exactly and that the $^3P_0$ LIF intensity is measured at a temperature uncertain by ±10K. At 3500K, the appropriate $^5D_0$ intensity by which the $^3P_0$ intensity should be divided is then uncertain by about 17%. Simultaneous measurements of the two intensities (with two lasers) would eliminate this effect and allow more precise population ratio measurements.

The equilibrium tungsten $^3P_0$:$^5D_0$ population ratio, R, is:

$$R = \exp\,[-13713/T(K)] \tag{37}$$

and the temperature may be calculated from measurements of R with a precision:

$$\Delta R/R = (13713/T)(\Delta T/T) \tag{38}$$

R measurements to ±1% should be possible by two laser techniques and, at 3500K, the temperature would then be fixed to ±9K. Appropriate calibration of the intensity ratio measurements would allow absolute temperatures to be calculated, with an accuracy and precision equivalent to that of optical pyrometry.

The calculation of temperature from the intensity ratio for two electronic states requires calibration of the intensity ratio at some known temperature. Experiments with two lasers can be designed so that absolute concentration ratios are obtained directly. Consider the case where two metastable states, $S_0$ and $S_1$, can be excited to the same upper level, $S_2$. Also, suppose $S_2$ can itself be excited to $S_3$ from which LIF is measured. In the two-laser experiment, one laser saturates the $S_0$-$S_2$ or the $S_1$-$S_2$ transition in a relatively large volume, within which the second laser produces LIF from $S_3$. With $I_0$ and $I_1$, the resulting intensity measurements, $n_0/n_1$, the concentration ratio of interest, and denoting multiplicities of the states by g, we have:

$$n_0/n_1 = (I_0/I_1)(g_0 + g_2)/(g_1 + g_2) \tag{39}$$

When $g_0 = g_1$, the intensity and concentration ratios are equal.

Velocity thermometry relates the mean thermal speed, c, of evaporating atoms to the surface temperature via:

$$c = (8kT/\pi m)^{\frac{1}{2}} \tag{40}$$

with a precision

$$\Delta c/c = 0.5(\Delta T/T) \tag{41}$$

Comparison of Eqs. (38) and (41) at, say, 3500K shows that the precision of velocity measurements must exceed that of electronic population ratios by about eight times if the two methods are to yield equally precise temperatures.

We obtained a supersonic levitation jet velocity equal to 394 ± 24 m/sec by measuring the fluorescence image position versus the delay time between the laser pulse and fluorescence detection. The low precision of this measurement is mainly due to the ±0.001 cm uncertainty in position measurements and the small image motion in the delay times interval (240 ns,

twice the Hg atom radiative lifetime) for which fluorescence was observable. We estimate that the velocity of evaporating tungsten atoms at 3500K could be measured to at least ±1% by observing time delayed fluorescence from long-lived upper states (see Table 5). However, a spatial filter would be necessary to improve the focusing properties of the visible dye laser beam, and more sensitive detection electronics would be necessary for such experiments.

A more sensitive and more widely applicable method for velocity measurements that does not require a large upper electronic state lifetime employs two lasers. Consider, for example, the transitions between tungsten $^3P_0$ or $^5D_0$ atoms and the upper energy level at E = 34,342 $cm^{-1}$. About 30% of the $^5D_0$ atoms pumped to this level emit to the $^3P_0$ state. A focused laser pulse at $\lambda$ = 291.1 nm would thus create a high concentration of metastable $^3P_0$ atoms in the region it intercepts. A subsequent laser pulse at $\lambda$ = 402.9 nm would re-excite the $^3P_0$ atoms to the 34,342 $cm^{-1}$ level and about half of the resulting fluorescence would occur at $\lambda$ = 291.1 nm. The time delay between the two laser pulses can be chosen to give, say, a 1-cm average displacement of $^3P_0$ atoms between creation and detection. The resulting velocity measurements would not be limited by spatial resolution effects, and can probably be made to much better than ±1%.

2. Tungsten and molybdenum evaporation: The measured and literature values agree for the enthalpy of W evaporation and are within the uncertainty of the measurements and of the optical pyrometer calibration for Mo evaporation. But the measurement errors are much larger than typical errors in the enthalpies of formation of many refractory materials. This is because the second law technique, which derives enthalpies from the temperature dependence of an equilibrium constant ($K_{eq}$) is inferior to the third law technique, which requires an absolute value of $K_{eq}$ at a given temperature, and calorimetric measurements of the reaction entropy. In the present study of tungsten evaporation, a 10K temperature error of opposite sign at either end of the pyrometer calibration interval (2890 to 3680K) produces a 2.7% error in the evaporation enthalpy. Even larger errors may be present due to the uncertainty in the melting points of Mo (±10K)[5] and W (±20K).[5] On the other hand, the temperature error required to produce a 2.7% error in the third law enthalpy for tungsten evaporation is nearly 100K at 3400K if there is no error in the equilibrium constant measurement.

3. $LaB_6$ evaporation: Eq. (33) is the fundamental basis for the thermodynamic analysis of $LaB_6$ results, which is based on the third law of thermodynamics. Thus, these results do not suffer the lack of precision inherent to second law analyses. Although the calculation of absolute concentrations from the measured self-absorption effect is complicated and tedious, it is as accurate as the $A_{21}$ values and the concentration and temperature gradients allow. The 25% uncertainty in $A_{21}$ values for the boron atom $^2S_{1/2}$-$^2P^o_{3/2,1/2}$ transitions is the principal source of error in the final result. This error would be negligible if, say, the delayed coincidence technique[6,30] were applied to measure the B-atom $^2S_{1/2}$ radiative lifetime.

An implicit assumption of our analysis is that the fraction of boron atoms that are excited to emit fluorescence is independent of temperature. This assumption is based on the facts that the nominal laser band width (0.8 $cm^{-1}$) is larger than the "Doppler half width" of the absorption line, which varies with temperature from approximately 0.29 to 0.39 $cm^{-1}$ at the point where LIF is excited. Also, the laser power (approximately $10^5$ $w/cm^2$) is very large compared to that required to saturate boron atom fluorescence. Thus, the fraction of atoms excited by the laser varies little over the absorption line or with temperature.

The lack of agreement between the present result and that obtained in the $LaB_6$ vaporization study reported by Storms and Mueller[26,27] provides indirect evidence that reaction with effusion cells is responsible for discrepancies in boron and boride vaporization studies. However, the enthalpy of boron vaporization is sufficiently uncertain (see Table 7) that further evidence in support of this hypothesis is needed. Such evidence is cited elsewhere[22] with reference to the recent effusion studies of elemental boron vaporization reported by Mar and Bedford[25] and Storms and Mueller.[28]

Crucible interactions have been a major difficulty in previous studies of boron and boride evaporation reactions. The present containerless method avoids such problems and may be applied to obtain thermodynamic results for boron and borides that evaporate congruently. To do so would require accurate spectral emittances for the materials of interest or application of one of the methods discussed earlier to measure accurate specimen temperatures. Earth-based research is sufficient for this purpose, and we have not proposed extension of the boride work in our NASA-sponsored research.

4. Containerless equilibrium component activity measurements: With accurate temperature measurements, containerless LIF experiments can achieve accurate third law measurements of reaction enthalpies. For binary compounds, the required data are activities of the elemental components. The activities can be directly measured by LIF as the ratio of fluorescence intensities over the material of interest and over the pure elements at the same temperature. Gas phase/ condensed phase equilibrium is required and would be achieved in vaccum evaporation experiments only for materials whose evaporation coefficients are unity. Unit evaporation coefficients are typical of metals and liquids. Thus, application of LIF to thermodynamic measurements on high temperature liquids is a promising application for containerless experiments.

Gas phase/condensed phase equilibrium can be insured by use of an ambient inert gas atmosphere that retards the evaporation rate. In spherical geometry, with a large container-to-specimen radius ratio, the diffusion limited evaporation rate, f, is:

$$f_D = 2Dn/d \tag{42}$$

where n = p/RT (p is the equilibrium vapor pressure), D is the binary diffusivity of the vapor specie in the ambient atmosphere, and d is the specimen diameter. In Knudsen effusion;

$$f_K = nca/4A \tag{43}$$

where $c = (8kT/\pi m)^{\frac{1}{2}}$ is the mean thermal speed of evaporating atoms or molecules and a/A is the ratio of effusion cell orifice area to the specimen surface area. Typical values are $a/A = 0.01$, $c = 5 \times 10^4$ cm/sec, $d = 0.3$ cm, and $Dp = 1.0$ $cm^2$ atm/sec (with p = total pressure) at, say, T = 2000K. Then, if the ambient pressure exceeds 0.05 atm, the rate of diffusion limited evaporation in the containerless experiment would be less than the rate of evaporation from a typical Knudsen effusion cell. Gas phase/condensed phase equilibrium should thus be easily obtained and verified by use of an inert gas to suppress evaporation by an amount that depends on the inert gas pressure.

## V. REFERENCES


1. Nordine, P. C. and R. A. Schiffman, "Containerless High Temperature Property Measurements by Atomic Fluorescence," First Annual Technical Report, NASA Contract NAS8-34383, Yale University, New Haven, Connecticut, October 1982.

2. Nordine, P. C., "Containerless High Temperature Property Measurements by Atomic Fluorescence," Second Annual Technical Report, NASA Contract No. NAS8-3483, Midwest Research Institute, Kansas City, Missouri, June, 1983.

3. Nordine, P. C. and R. M. Atkins, "Aerodynamic Levitation of Laser-Heated Solids in Gas Jets," Rev. Sci. Instrum., 53, 1456 (1982).

4. Nordine, P. C., R. A. Schiffman, and D. S. Sethi, "Atomic Fluorescence Study of High Temperature Aerodynamic Levitation," in G. E. Rindone, ed., Materials Processing in the Reduced Gravity Environment of Space, Elsevier, New York, 1982, pp. 43-48.

5. Hultgren, R., P. D. Desai, D. T. Hawkins, M. Gleiser, K. K. Kelley, and D. D. Wagman, "Selected Values of the Thermodynamic Properties of the Elements," Am. Soc. for Metals, Metals Park, Ohio (1973).

6. G. C. King and A. Adams, "An Accurate Determination of the Lifetime of the $6^3P$ state in Mercury Using a new Electron-Photon Delayed Comcidence Apparatus," J. Phys. B:Atom. molec. Phys. 7, 1712-1718 (1974).

7. Meggers, W. F., C. H. Corliss, and B. F. Scribner, Tables of Spectral-Line Intensities Part I - Arranged by the Elements, NBS Publication MN-145, USGPO, Washington, D.C., 1975.

8. Bier, K. and B. Schmidt, Z. Angew. Phys., 13, 34 (1961); H. Ashkenas and F. S. Sherman, Proc. 4th Int. Symp. on Rarefied Gas Dynamics, J. H. DeLecuw, ed., Academic Press, New York (1966), Vol. 2, p. 84; S. Christ, P. M. Sherman, and D. R. Glass, AIAA J, 4, 68 (1966).

9. Stull, D. R. and H. Prophet, JANAF Thermochemical Tables, 2nd Ed., USGPO, Washington, D.C. (1971); M. W. Chase, J. L. Curnutt, R. A. McDonald, and A. N. Sevrud, J. Phys. Chem. Ref. Data, 7, 793-940 (1978).

10. Grvnak, D. A. and D. E. Burch, "Optical and Infrared Properties of $Al_2O_3$ at Elevated Temperatures," J. Opt. Soc. Amer., 55, 625-629 (1965).

11. Nordine, P. C., E. H. Lee, and J. L. Hurd, "Spectral Emittance of Polycrystalline Alumina," Rev. int. hautes Temper. Refract., 17, 165-171 (1980).

12. Van Audenhove, J., "Vacuum Evaporation of Metals by High Frequency Levitation Heating," Rev. Sci. Instrumen., 36, 383-385 (1965).

13. Moore, C. E., Atomic Energy Levels, I, II, III, USGPO Washington, D.C. (1971).

14. Espe, W., Materials of High Vacuum Technology Vol. 1, Metals and Metalloids, Pergamon Press, New York (1966).

15. Storms, E. K., "The Emissivity of $LaB_6$ at 650 nm," J. Appl. Phys., 50, 4450 (1979).

16. Ting, Y., "Hyperfine Structure and Quadrupole Moment of $^{139}La$," Phys. Rev., 108, 295-304 (1957).

17. Childs, W. J., and L. S. Goodman, "Hyperfine Structure of Excited, Odd-Parity Levels in $^{139}La$ by Laser-Atomic Beam Fluorescence," J. Opt. Soc. Am., 68, 1348-1350 (1978).

18. Mitchell, A. C. G., and M. W. Zemansky, Resonance Radiation and Excited Atoms, Cambridge University Press, London (1934).

19. Weiss, A. W., Phys. Rev., 188, 119 (1969).

20. Bergström, I., J. Bromander, R. Buchta, L. Lundin, and I. Martinson, Phys. Lett., 28A, 721 (1969).

21. Lewis, G. N., and M. Randall, Thermodynamics, 2nd ed. (revised by K. S. Pitzer and L. Brewer), McGraw Hill, New York (1961).

22. Nordine, P. C., and R. A. Schiffman, "Containerless Laser Induced Fluorescence Study of $LaB_6$ Evaporation," High Temp. Science (accepted).

23. Topor, L., and O. J. Kleppa, J. Chem. Thermodynamics (to be published).

24. JANAF Thermochemical Data, Dow Chemical Company, Midland, Michigan (revised boron data sheets), March 31, 1979.

25. Mar, R. W., and R. G. Bedford, "The Sublimation of Boron," High Temp. Science, 8, 365 (1976).

26. Storms, E., and B. Mueller, "Phase Relationship, Vaporization, and Thermodynamic Properties of the Lanthanum-Boron System," J. Phys. Chem., 82, 51 (1978).

27. Storms, E. K. (private communication, 1984). The value given in Ref. 26 for the standard enthalpy of $LaB_6$ formation is not consistent with the stated activities, which are correctly recorded. The correctly calculated result is $\Delta H^{o}_{f,298}$ ($LaB_6$) = -254 ± 8 kJ/mol.

28. Storms, E., and B. Mueller, "Phase Relationships and Thermodynamic Properties of Transition Metal Borides. 1. The Molybdenum-Boron System and Elemental Boron," J. Phys. Chem., 81, 318-324 (1977).

29. Kwiatkowski, M., G. Micali, K. Werner, and P. Zimmermann, "Radiative Lifetimes and Oscillator Strengths in MoI," Phys. Lett., 85A, 273-274 (1981).

30. Imhoff, R. E., and M. H. Reed, Rep. Prog. Phys., 40, 1-103 (1977).

## VI. PUBLICATIONS AND PRESENTATIONS


Nordine, P. C., and R. M. Atkins, "Aerodynamic Levitation of Laser-Heated Solids in Gas Jets," Rev. Sci. Instrum., 53, 1456-1464 (1982).

Nordine, P. C., R. A. Schiffman, and D. S. Sethi, "Atomic Fluorescence Study of High Temperature Aerodynamic Levitation," in G. E. Rindone, ed., Materials Processing in the Reduced Gravity Environment of Space, Elsevier Science Publishing Company, New York, 1982, pp. 43-48.

Nordine, P. C., and R. A. Schiffman, "Containerless Laser Induced Fluorescence Study of $LaB_6$ Evaporation," High Temp. Science (accepted for publication).

Schiffman, R. A., and P. C. Nordine, "Laser Induced Fluorescence Study of $Al_2O_3$ Evaporation and High Temperature Gas Thermometry" (in preparation).

Nordine, P. C., and R. A. Schiffman, "Laser Induced Hg ($^3P_1$) Fluorescence Study of a Supersonic Free Jet" (in preparation).

Nordine, P. C., and R. A. Schiffman, "LIF Study of W and Mo Vaporization" (in preparation).

Nordine, P. C., "Chemical Reaction Studies with Laser Induced Fluorescence," presented at the NASA Containerless Processing Meeting, Arlington, Virginia, October 21-22, 1982.

Nordine, P. C., "Containerless High Temperature Property Measurements by Laser Induced Fluorescence," Materials Science in Space Seminar, Presented at NASA-Lewis Research Laboratory, November 3, 1982.

Schiffman, R. A., and P. C. Nordine, "Pulsed Laser Fluorescence Study of Evaporating Metals," Presented at the 1983 TMS-AIME Annual Meeting, Atlanta, Georgia, March 6-10, 1983.

Nordine, P. C., and R. A. Schiffman, "Laser Induced Fluorescence Study of Reactions on Levitated Materials," Presented at the Midwest High Temperature Chemistry Conference, Lawrence, Kansas, June 9-11, 1983.

Schiffman, R. A., "Temperature Measurement by Laser Induced Fluorescence," Presented at the Midwest High Temperature Chemistry Conference, Lawrence, Kansas, June 9-11, 1983.

Nordine, P. C., "Laser-Induced Fluorescence Studies of Ceramics at High Temperatures," Presented at Lawrence Livermore National Laboratory, Livermore, California, July 18, 1983.

Nordine, P. C., and R. A. Schiffman, "Containerless Laser-Induced Fluorescence Study of Vaporization Reactions," presented at The Fourth International IUPAC Conference on High Temperature and Energy-Related Materials, Santa Fe, New Mexico, April 2-6, 1984.

## VII. DISTRIBUTION

NASA

Marshall Space Flight Center, Alabama 35812

1. Mail Code AP35 (M.A. Kelly)
2. Mail Code AP35D (T. P. Crabb)
3. Mail Code ASD21 (3 copies)
4. Mail Code AT01
5. Mail Code LA02 (W. H. Savage)
6. Mail Code ES74 (E. Ethridge)
7. Mail Code JA64 (L. B. Gardner) (20 copies plus reproducible copy)

8.
DCASD: Fred Walters, Administrative Contracting
Officer, Office of Naval Research,
715 Broadway - 5th Floor, New York, NY 10003

NASA Headquarters

9. Mail Code EM-7 (R. E. Halpern)
10. Mail Code EM-7 (W. Oran) {Washington, D.C. 20546

11. Dr. Martin B. Barmatz
Jet Propulsion Laboratory
California Institute of Technology
4800 Oak Grove Drive
Pasadena, CA 91103

12. Dr. David Bonnell
National Bureau of Standards
4329/223 Division 561
Washington, D.C. 20234

13. Prof. Leo Brewer
Department of Chemistry
University of California-Berkeley
Berkeley, CA

14. Prof. Rointan F. Bunshah
Department of Materials Science & Engineering
School of Engineering & Applied Science
65323 Boelter Hall - UCLA
Los Angeles, CA 90024

15. Dr. Robert T. Frost
General Electric Company
P.O. Box 8555
Philadelphia, PA 19101

16. Prof. Paul W. Gilles
Department of Chemistry
University of Kansas
Lawrence, KS 66045

17. Dr. Clarence Hoenig
Ceramic Technology Group
Chemistry and Materials Science Dept.
Lawrence Livermore National Laboratory
P.O. Box 808
Livermore, CA 94550

18. Dr. Fred J. Kohl
National Aeronautics & Space Administration
Lewis Research Center, M.S. 106-1
Cleveland, OH 44135

19. R. Landingham, L369
Chemistry and Materials Science Department
Lawrence Livermore National Laboratory
P.O. Box 808
Livermore, CA 94550

20. Prof. John Margrave
Department of Chemistry
Rice University
P.O. Box 1892
Houston, TX 77001

21. Dr. Robert A. Sallach
Sandia Laboratories
Albuquerque, NM 87185

22. Dr. Jerry J. Smith
Office of Naval Research
Chemistry Programs
Arlington, VA 22217

23. Prof. C. A. Walker
Department of Chemical Engineering
Yale University
2059 Yale Station
New Haven, CT 06520

24. Dr. Terry C. Wallace
Los Alamos Scientific Laboratory
Los Alamos, NM 87545

25. Dr. E. G. Zubler
General Electric Company
Nela Park #1310
Cleveland, OH 44112